Supporting Information

Adsorptive Removal of Iodate Oxyanions from Water using a Zr-based Metal–Organic Framework

Christopher Copeman,[a] Hudson A. Bicalho,[a] Maxwell W. Terban,[b] Diego Troya,[c] Martin Etter,[d] Paul L. Frattini,[e] Daniel M. Wells,[e] Ashlee J. Howarth*[a]

[a]Department of Chemistry and Biochemistry, and Centre for NanoScience Research, Concordia University, 7141 Sherbrooke St W., Montreal, QC, H4B 1R6, Canada.

[b]Max Planck Institute for Solid State Research, Heisenbergstraße 1, 70569 Stuttgart, Germany

[c]Department of Chemistry, Virginia Tech, Blacksburg, Virginia 24061, United States

[d] Deutsches Elektronen-Synchrotron DESY, Notkestraße 85, 22607Hamburg, Germany

[e]Electric Power Research Institute Inc., 3420 Hillview Ave, Palo Alto, CA 94304, United States

Corresponding author email: ashlee.howarth@concordia.ca.

Materials

All materials were purchased from commercial sources. *N,N*-dimethylformamide (DMF), acetone, hydrochloric acid and ammonium hydroxide were purchased from Fisher Scientific. Zirconyl chloride octahydrate ($ZrOCl_2 \cdot 8H_2O$), 1,3,5-benzenetricarboxylic acid (H_3BTC), 97% formic acid and potassium iodate were purchased from Alfa Aesar. ICP standards were purchased from Inorganic Ventures. All the water used in this study is Millipore Milli-Q 18.2 MΩ·cm.

Characterization

Powder X-ray diffraction (PXRD) patterns were collected on a Bruker D8 Advance diffractometer (measurement made over a range of $3° < 2\theta < 40°$ in 0.02° step with a 0.200 s scanning speed) equipped with a LYNXEYE linear position sensitive detector (Bruker AXS, Madison, WI). Neat samples were smeared directly onto the silicon wafer of a proprietary low-background sample holder. Data was collected using a continuous coupled θ/2θ scan with Ni-filtered CuKα (λ = 1.54178 Å radiation operating at 40 kV and 40 mA).

^{1}H-NMR spectra were collected with a 300 MHz Bruker spectrometer. Chemical shifts were referenced to the residual solvent peaks. Approximately 2 mg of MOF-808 was digested in 8 drops of D_2SO_4 before dilution in 0.6 mL DMSO-d_6.

Diffuse reflectance infrared spectra were collected using a Thermo Scientific Nicolet 6700 FT-IR equipped with a liquid nitrogen cooled MCT detector with a resolution of 1 cm^{-1}.

Scanning electron microscopy (SEM) images and energy dispersive X-ray spectroscopy data were collected on a Phenom ProX desktop SEM.

MOF samples were activated using a Micromeritics SmartVacPrep instrument equipped with a hybrid turbo vacuum pump. Nitrogen adsorption-desorption isotherms were measured at 77 K on a Micromeritics TriStar II Plus instrument. BET surface areas are calculated using isotherm points between 0.0005 and 0.1 P/P_0 that satisfy all BET criteria.

Inductively coupled plasma – mass spectrometry (ICP-MS) data was measured on an Agilent 7500 Series. Standards were prepared at concentrations of 0.05, 0.1, 0.2, 0.5 and 1 ppm I^- by serial dilution in a 0.5% (v/v) solution of ammonium hydroxide.

Water Stability of MOF-808

MOF-808 is stable in water, however, the framework can be sensitive to repeated adsorption and desorption of water vapor.[1] Stability to repeated water vapor adsorption and desorption does not necessarily relate to stability in aqueous solutions. The framework collapse that occurs after the desorption of water in these experiments is a result of capillary forces exerted on the MOF. This does not occur when the MOF is submerged in the aqueous environments we describe, where the main pathway for structural collapse is linker hydrolysis.[2] For this reason, the MOF is always washed 3x with acetone before drying after the MOF has been submerged in aqueous solutions. The water stability of MOF-808 has led to a variety of studies for applications in aqueous environments.[3,4,5,6,7,8,9,10]

Experimental/Methods

MOF-808 was synthesized using a modified procedure[3] by combining 97 mg of $ZrOCl_2 \cdot 8H_2O$ with 63 mg of H_3BTC in 7.5 mL each of DMF and formic acid. The resulting mixture was sonicated until the components were dissolved and placed in an oven at 120 ^oC to react for 72 hours. The MOF was washed three times with fresh DMF (3 x 10 mL) and soaked in fresh DMF (10 mL) overnight, followed by three acetone washes (3 x 10 mL) and an overnight acetone (10 mL) soak. The powder was subsequently dried in a vacuum oven at 80 ^oC before soaking in 10 mL of 0.1 M HCl overnight to remove the formate capping ligands from the MOF nodes. The MOF was centrifuged and the HCl solution was removed followed by three water washes (3 x 10 mL), and three acetone washes (3 x 10 mL). The MOF was soaked in acetone (10 mL) overnight before drying in a vacuum oven at 80 ^oC for one hour, and then activated on a Micromeritics SmartVacPrep at 120 ^oC for 20 hours. 45.4 mg of sample was activated and used to collect the isotherm appearing in Figure S3.

<u>Maximum iodate uptake per node</u>

2.5 mg of activated MOF-808 was placed in a 15 mL centrifuge tube with 10 mL of either 41, 82, 123, 164, 205, 246, or 287 ppm solution of potassium iodate, corresponding to an exposure of 2, 3, 4, 5, 6, and 7 iodate anions per metal node of MOF. After 72 hours, the solutions were centrifuged to settle the MOF. 50 µL aliquots were taken and diluted to 5 mL with 0.5% ammonium hydroxide. The iodine concentration in each sample was determined by ICP-MS and compared to that of the corresponding stock solution to determine the iodate uptake by the MOF. A basic matrix for iodate samples is required to prevent the formation of volatile I_2 which can permeate polypropylene, causing memory effects and incorrect concentration measurements.[11]

Iodate uptake kinetics experiments

2.5 mg of activated MOF-808 was placed in a 15 mL centrifuge tube with 10 mL of either 41, 61.5, 82, 102.5, or 123 ppm solution of potassium iodate, corresponding to exposure of 1, 1.5, 2, 2.5, and 3 iodate molecules per node of MOF. The solution was centrifuged for 3 minutes for the MOF to settle, before aliquots of the supernatant were taken at 4, 6, 8, 10, 20, 40, 60, 120, and 180 minutes, as well as 24, 48 and 72 hours after initial exposure. The concentration of iodine was measured by ICP-MS, where the samples were diluted 100-fold with a 0.5% ammonium hydroxide solution by adding 50 µL aliquots to 5 mL.

The adsorption (q) in mg/g was determined for each exposure concentration performed using equation 1, where C_i is the initial concentration (ppm), C_f is the final concentration (ppm), V is the volume (L) of iodate solution, and m is the mass (g) of MOF used. The maximum equilibrium adsorption capacity (Q) was determined by fitting the data to the Langmuir adsorption model. The Langmuir equation (Equation 2) was used to determine the Q for iodate uptake in MOF-808, where C_e is the equilibrium adsorption concentration (ppm) taken as the average of the concentrations at 48, 72 and 96 hours, and q_e is the equilibrium uptake (mg/g), taken as the average of the calculated q values at 48, 72, and 96 hours.

Equation 1: $q = (C_i - C_f) \times V/m$

Equation 2: $C_e/q_e = (1/Q)C_e + 1/K_LQ$

Regeneration Experiments

To test the reusability of MOF-808 in multiple adsorption cycles, 10 mg of MOF-808 was exposed to 10 mL of a 1148 ppm solution (7 iodate anions/node) of potassium iodate overnight. The MOF powder and iodate solution was then placed on a membrane filter in a glass microfiltration apparatus attached to a vacuum pump. The iodate solution was drawn through the membrane, the filtrate collected, and the MOF on the membrane was washed with 3 x 10 mL of water. 10 mL of 1%, 3%, 5%, or 10% HCl was then drawn through the MOF sample over the course of 5 minutes by vacuum control. Aliquots (100 µL) of the acid filtrate were taken immediately after filtration and diluted 2000x by serial dilution with 0.5% ammonium hydroxide. The iodine concentration was measured

via ICP-MS to determine the amount of iodate removed from the MOF by the acid wash. After washing with acid, the MOF on the membrane was again washed with 3 x 10 mL of water. The powder was then placed in a fresh solution of 1148 ppm potassium iodate to soak overnight and begin the next adsorption cycle. Three adsorption-desorption cycles were performed.

To assess the porosity after recycling, 5 batches of 10 mg MOF-808 were loaded with iodate and regenerated with 10% HCl as described above. After the 3rd cycle, the MOF samples were combined and washed 3x with 20 mL of water, and 3x with 20 mL of acetone and left to soak in acetone overnight before activation and BET measurement.

To assess the porosity of MOF-808 after adsorption, 50 mg of MOF-808 was exposed to 50 mL of a 1148 ppm (7 iodate anions/node) solution of potassium iodate overnight. Iodate loaded samples were then washed 3x with 20 mL of water, and 3x with 20 mL of acetone and left to soak in acetone overnight before activation and BET measurement.

For the nitrogen adsorption-desorption isotherms appearing in Figure 5b, 234.0 mg, 20.1 mg, and 33.2 mg of MOF was used for analysis of MOF-808, MOF-808 + Iodate, and HCl regenerated MOF-808, respectively.

Density Functional Theory Calculations

Density functional theory geometry optimization calculations were performed on MOF-808 Zr_6 node models in order to determine the mode of iodate anion binding. Models consisted of either a single metal node with 6 benzoate truncated linkers, or dual node model with two bridging benzene dicarboxylate type linkers, and remaining dangling linkers truncated to benzoate. To mimic the crystal environment of the MOF, all linker carbon atoms were frozen. Optimization calculations were performed with the B97D method and the def2-SVP basis set using the W06 density fitting set as implemented in Gaussian09. An ultrafine integration grid was used in all calculations.[12]

Total scattering experiments

X-ray total scattering measurements were conducted using beamline P02.1 of Petra III at the Deutsches Elektronen-Synchrotron (DESY), in Hamburg, Germany. Data were collected in a rapid acquisition mode[13] using a 2D VAREX XRD4343CT detector (2880 × 2880 pixels, 150 × 150 μm^2 each) mounted orthogonal to the beampath. The samples were packed in 1 mm diameter glass capillaries and measured with a sample-to- detector distance of 499.0 mm. The incident energy of the X-ray beam was 59.58 keV (λ = 0.20729 Å). LaB_6 was used to calibrate the detector position. The damping of data in real space due to the instrumental resolution in reciprocal space was characterized by fitting the structure of the calibration standard in the program PDFgui:[14] Q_{damp} =0.0170 $Å^{-1}$.

Data reduction

Calibration of the detector geometry and image integration were performed using the azimuthal integration software pyFAI.[15] The raw data images were summed and corrected for polarization effects, then masked and azimuthally integrated to produce 1D powder diffraction patterns. Further normalization and transformation to the real space PDF was performed using PDFgetX3 within xPDFsuite.[16,17] The total scattering structure function S(*Q*) is obtained from the coherent scattering intensities $I_c(Q)$, after removal of the self-scattering by,

$$S(Q) = \frac{I_c(Q)/N - \langle f(Q)^2 \rangle + \langle f(\mathrm{Q}) \rangle^2}{\langle f(\mathrm{Q}) \rangle^2}$$

Q is the magnitude of the scattering momentum transfer ($Q = 4\pi \sin(\theta)/\lambda$ for elastic scattering, where λ is the wavelength, and 2θ is the scattering angle). $f_i(Q)$ is the atomic form factor for atom *i*, and averaging denoted by $\langle . \rangle$ is performed stoichiometrically over all atoms (*N*) in the sample. The reduced total structure function is defined as

$$F(Q) = Q[S(Q) - 1]$$

and the experimental PDF, G(r), is obtained via truncated Fourier transformation,

$$G(r) = \frac{2}{\pi} \int_{Q_{min}}^{Q_{max}} F(Q) \sin(Qr)\, dQ$$

which corresponds to the real space density distribution by

$$G(r) = 4\pi r [\rho(r) - \rho_0 \gamma_0]$$

where ρ_0 is the average atomic number density and $\rho(r)$ is the local atomic pair density, which is the average density of neighboring atoms at a distance *r* from an atom at the origin. γ_0 is the characteristic function of the diffracting domains which equals 1 for bulk crystals, but has an *r*-dependence for nanosized domains.[18] The PDFs were determined with values of Q_{max} = 20.7 Å^{-1}. Simulated PDFs were determined from cluster models using the Debye function calculator in the Diffpy-CMI software,[16] using a Q_{range} = 0.5–20.0 Å^{-1} and B_{iso} = 0.5 Å^2.

Difference analysis

For the difference PDF analysis, a modification function *M*(*Q*)[19] was multiplied by *F*(*Q*) prior to the Fourier transformation (Q_{max} = 20.7 Å^{-1}) to minimize the presence of termination effects in the real-space signal. In order to assess the systematic errors introduced by the difference PDF (dPDF) extraction method used, the dPDF was extracted using four different subtraction methods:

1. Direct subtraction of empty MOF from loaded MOF intensities in reciprocal space
2. Subtraction in real space by optimizing the scale of empty and loaded MOF PDFs over a range of 1.5–6 Å
3. Subtraction in real space by fitting the empty to loaded MOF PDF: empty MOF PDF was modified by a spherical domain damping function, and a damped sine wave was added and refined to adjust for atomic density differences[20]
4. Same as above: the empty MOF PDF was additionally modified by an expansion coefficient to allow the signal to expand/contract to best fit the loaded MOF PDF signal[21]

Systematic uncertainties in the experimental dPDFs were then estimated as the standard deviations between the four different extraction methods. The model dPDFs were simulated from the clusters considering atom-pairs between I atoms and O atoms of the IO_3 motif (not bound to the cluster) with each other and with the rest of the atoms. The Debye function calculator in Diffpy-CMI software,[7] was used with a Q_{range} = 1.0–20.0 $Å^{-1}$ and B_{iso} = 1.0 $Å^2$.

Additional diffraction measurements

For verification of the sample structures, additional measurements were performed on the samples using a STOE Stadi-P diffractometer with CuKα radiation (λ = 1.540596 Å, a Ge(111) Johann monochromator, and a single Mythen detector scanned over a range of 0.0–115.0° 2θ over a timespan of approx. 3.7 hours. The samples were loaded into 0.7 mm diameter borosilicate capillaries, and the samples were spun during the measurement for optimal orientational sampling of the powdered crystallites.

Pawley and Rietveld refinements

Pawley and Rietveld refinements were performed using TOPAS v5/v6.[22] In either case, refinements were performed considering the cubic *Fd−3m* symmetry along with Gaussian and Lorentzian contributions to the peak profile broadening, and the Stephens model for strain (3 parameters). Further corrections included a zero-offset correction, sample length parameter in the full axial model for peak asymmetry, and the Lorentz-Polarisation factor for the given radiation and monochromator. The complicated backgrounds were described using combinations of Chebychev polynomials and broad Gaussian peaks or using a second *hkl* phase with a fixed peak broadening set to 1 nm. Additional pseudoatoms with atomic displacement parameters fixed to a larger value were included to account for pore water content and bound water or IO_3.

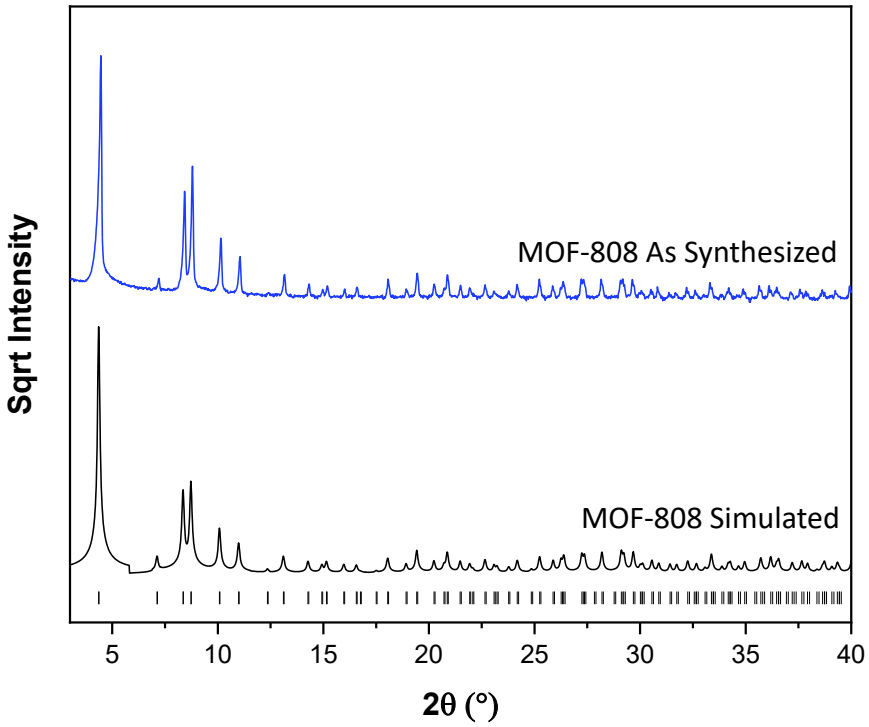

Figure S1. Powder X-ray diffraction patterns for as-synthesized MOF-808 compared to a simulated pattern.

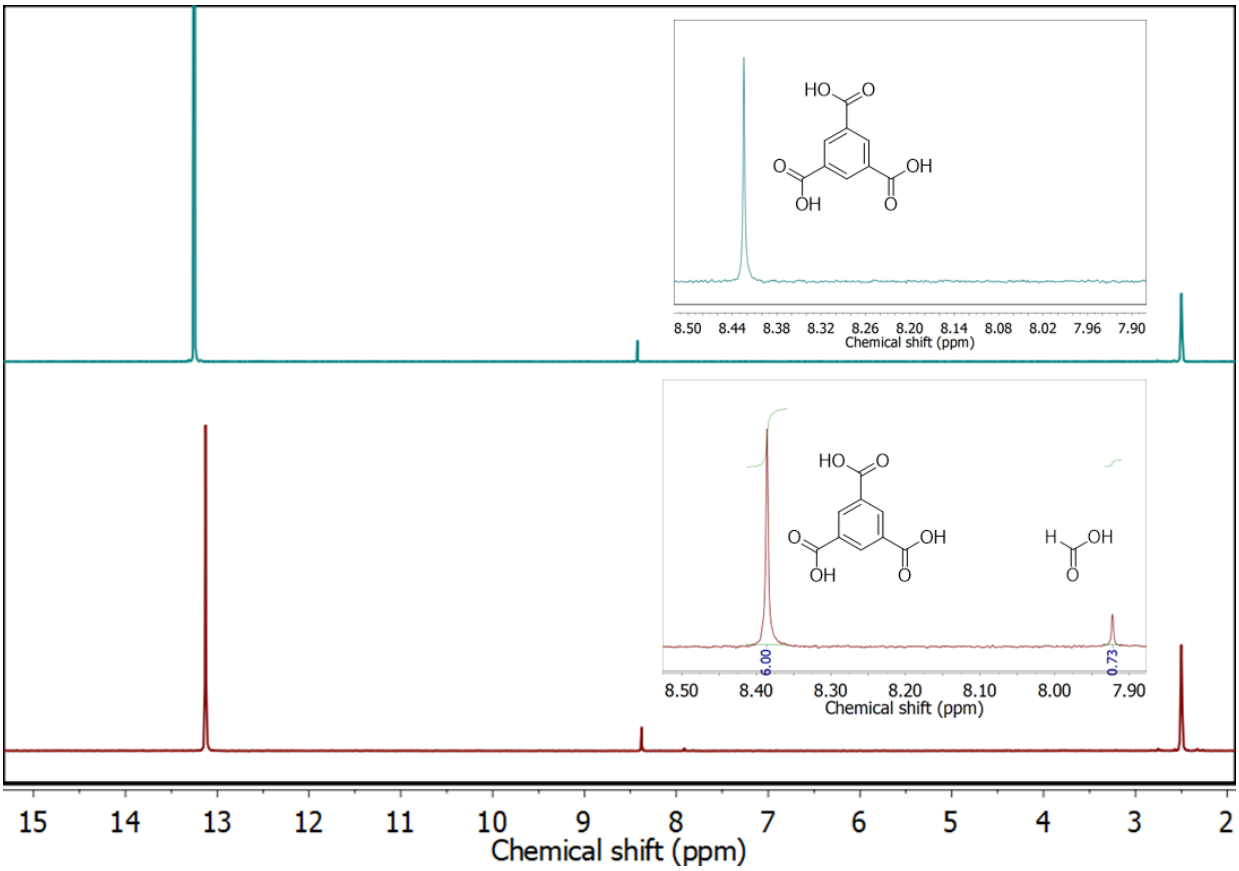

Figure S2. ^{1}H-NMR spectrum indicating the removal of node-bound formate from MOF-808.

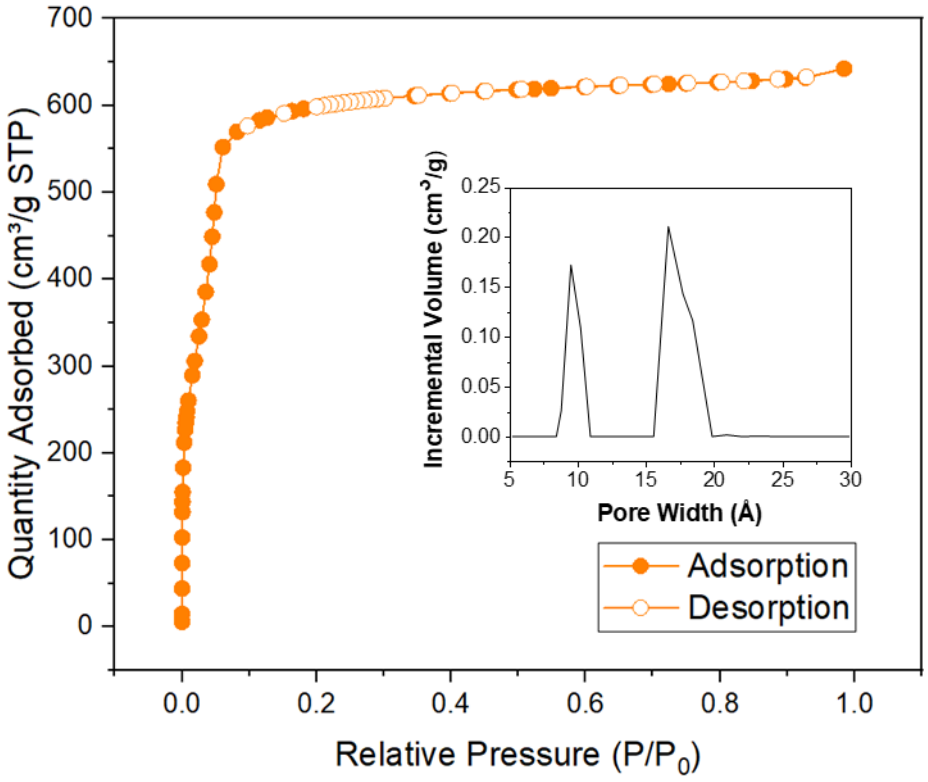

Figure S3. Nitrogen adsorption-desorption isotherm for as-synthesized MOF-808 at 77 K. MOF-808 pore size distribution inset.

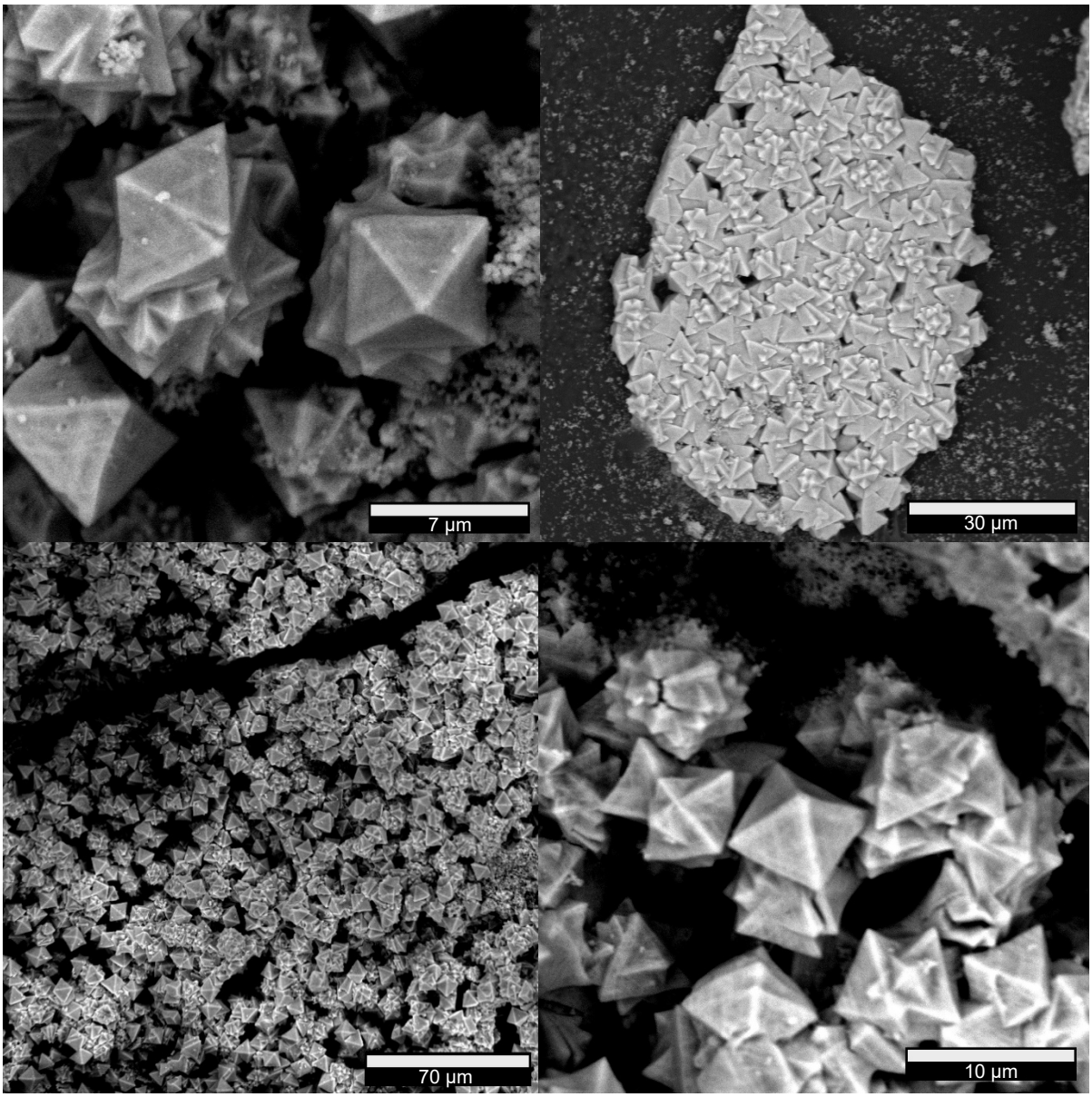

Figure S4. SEM images of as-synthesized MOF-808 crystallites.

Table S1. Iodate adsorption per gram and per node of MOF-808, after exposure to increasing concentrations of potassium iodate for 72 hours.

Exposure per node	72 h Uptake (mg/g)	Uptake per node
2	134	0.95
3	178	1.27
4	187	1.32
5	225	1.56
6	234	1.63
7	286	1.93

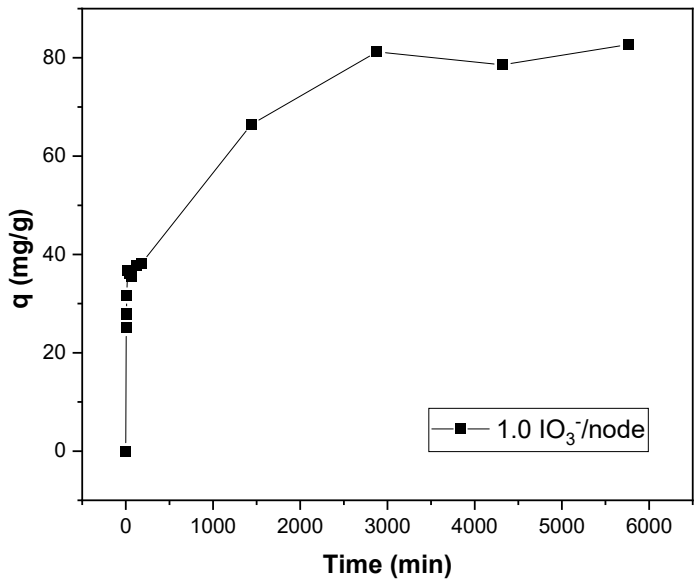

Figure S5. Iodate uptake vs time in MOF-808 when exposed to 1.0 iodate per node, 41.0 ppm KIO_3.

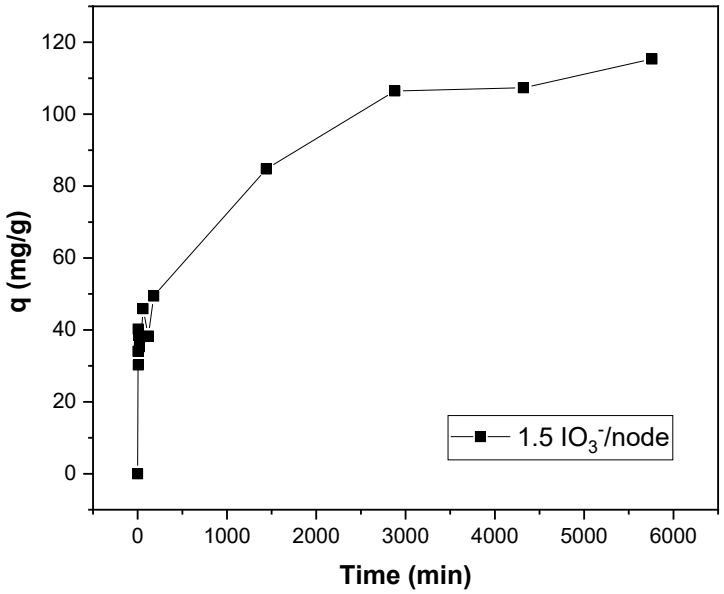

Figure S6. Iodate uptake vs time in MOF-808 when exposed to 1.5 iodate per node, 61.5 ppm KIO_3.

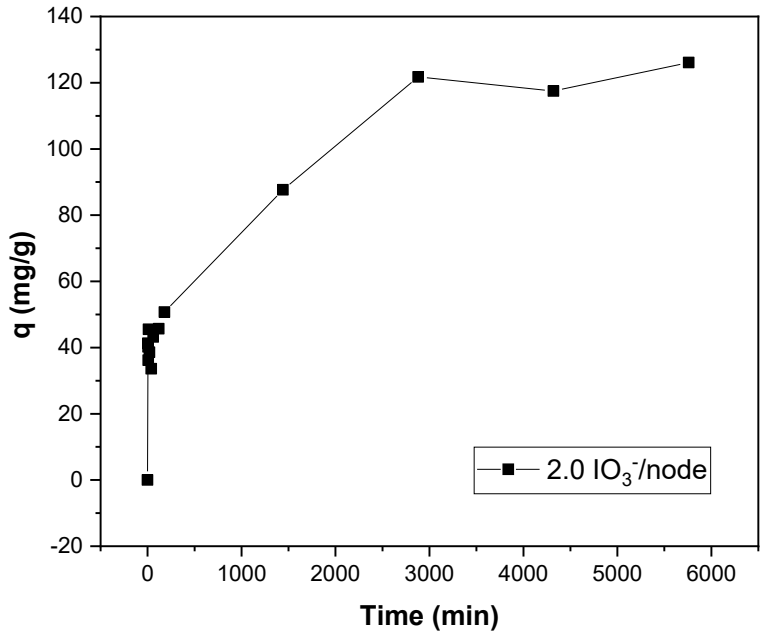

Figure S7. Iodate uptake vs time in MOF-808 when exposed to 2.0 iodate per node, 82.0 ppm KIO_3.

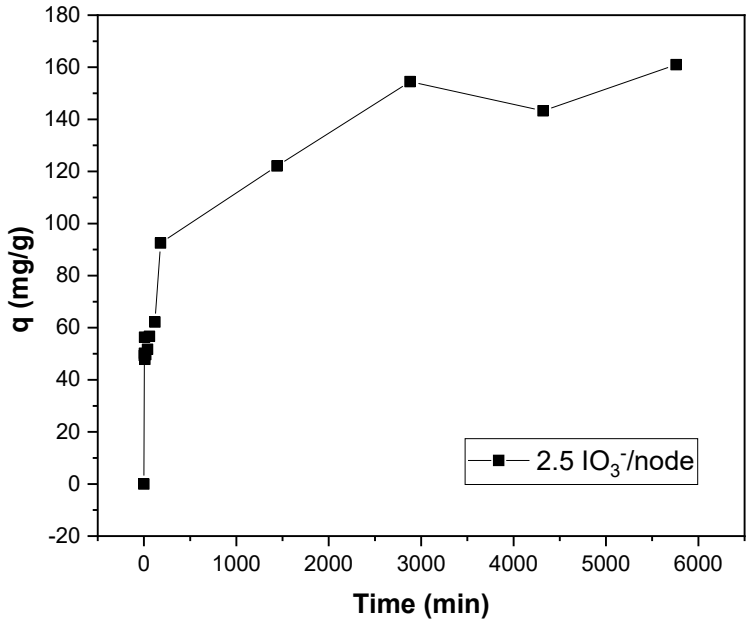

Figure S8. Iodate uptake vs time in MOF-808 when exposed to 2.5 iodate per node, 102.5 ppm KIO_3.

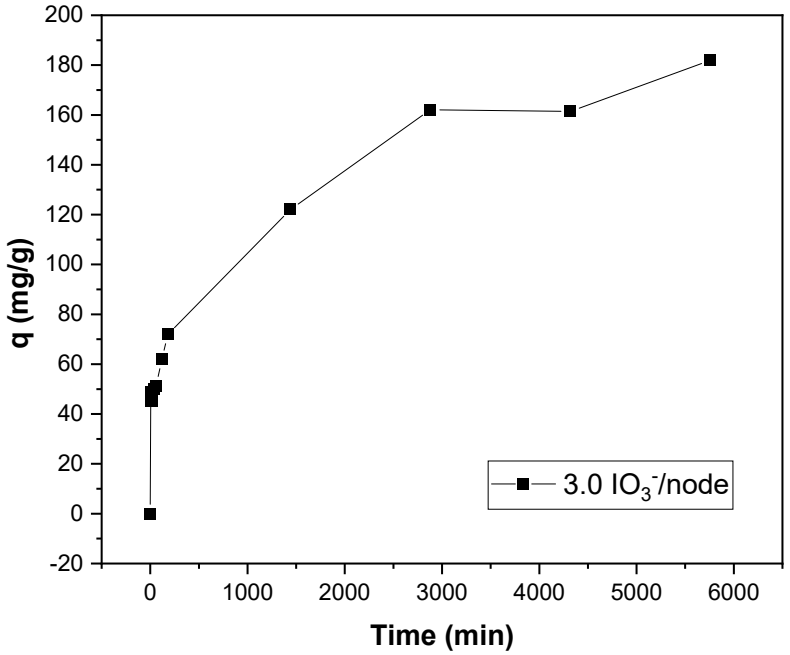

Figure S9. Iodate uptake vs time in MOF-808 when exposed to 3.0 iodate per node, 123.0 ppm KIO_3.

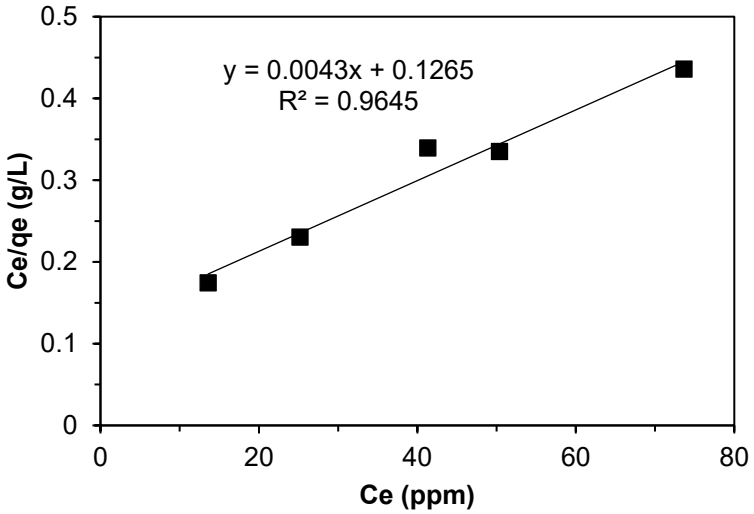

K_L (L/mg)	Q (mg/g)	R^2
0.034	233	0.9645

Figure S10. Langmuir plot for the adsorption of iodate in MOF-808.

Table S2. Iodate adsorption in various materials reported previously in the literature.

Material	**Uptake (mg/g)**	**Time**	**Concentration**	**Ref.**
Pomelo Peels	6.91	5 days	100 ppm	23
δ-Bi_2O_3@PES	170.6	5 hours	10-500 ppm	24
Hydrothermal Biochar	16.87	5 days	5-90 ppm	25
Diatomite/nano titanium dioxide	370 mL/g (Freundlich model)			17
Tubular Hallyosite	3.4	36 hours	17.5 ppm	26
Organoclays	21.1-27.5	6 days	8.75-875 ppm	27
Activated Carbon F400	40.25	24 hours	17.5-175 ppm	28
Chinese Soils	0.01-0.03	40 hours	1.3-11 ppm	29

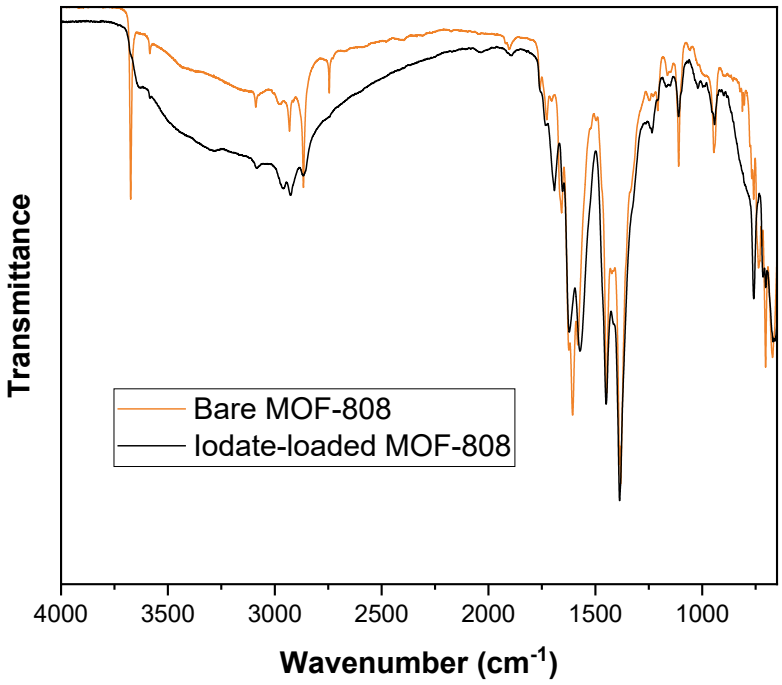

Figure S11. Diffuse reflectance infrared Fourier transform spectra of bare and iodate-loaded MOF-808.

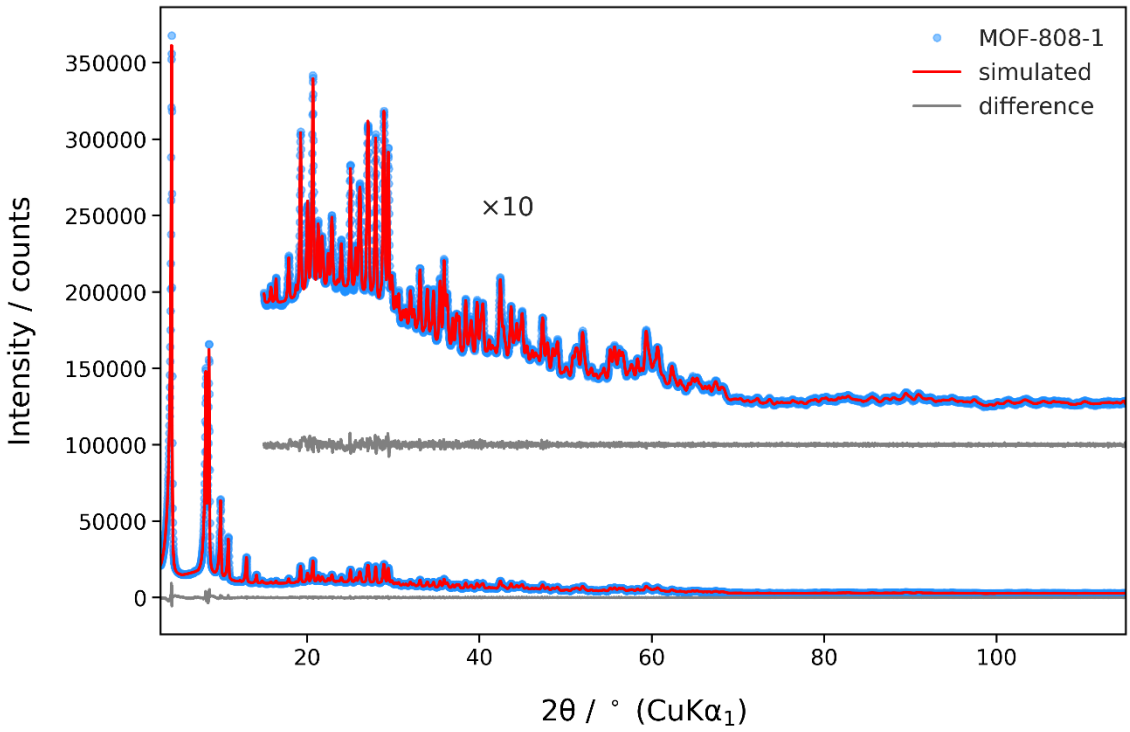

Figure S12. Pawley refinement of bare MOF-808 X-ray total scattering data.

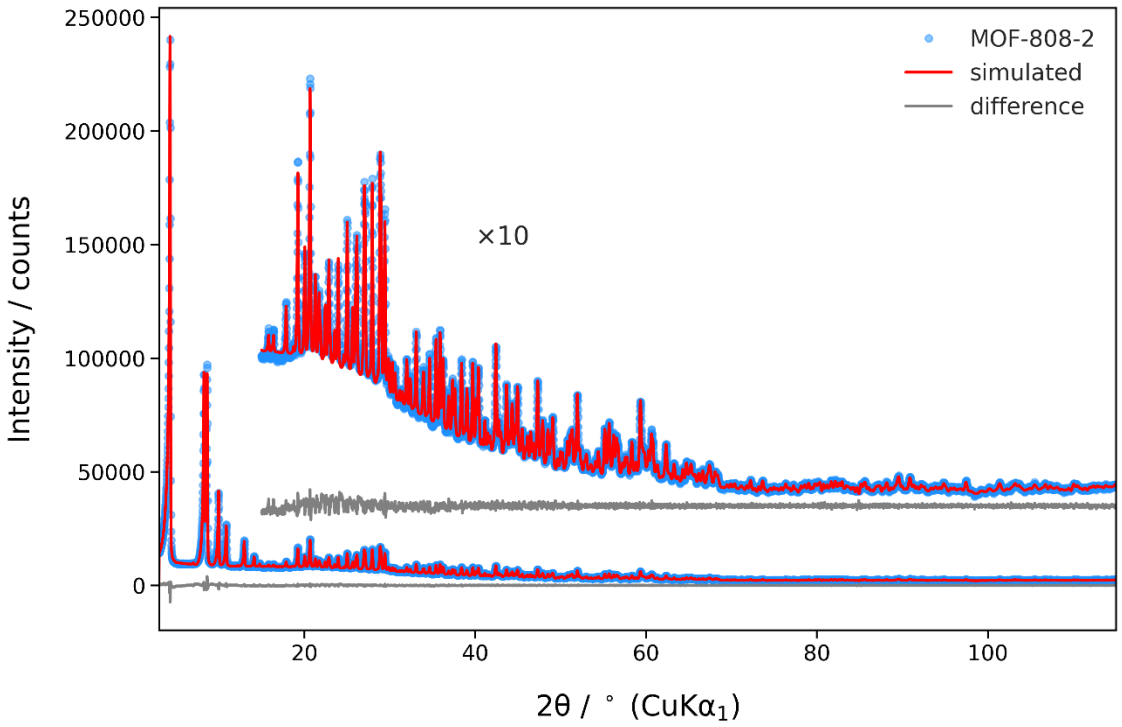

Figure S13. Pawley refinement of iodate-loaded MOF-808 X-ray total scattering data.

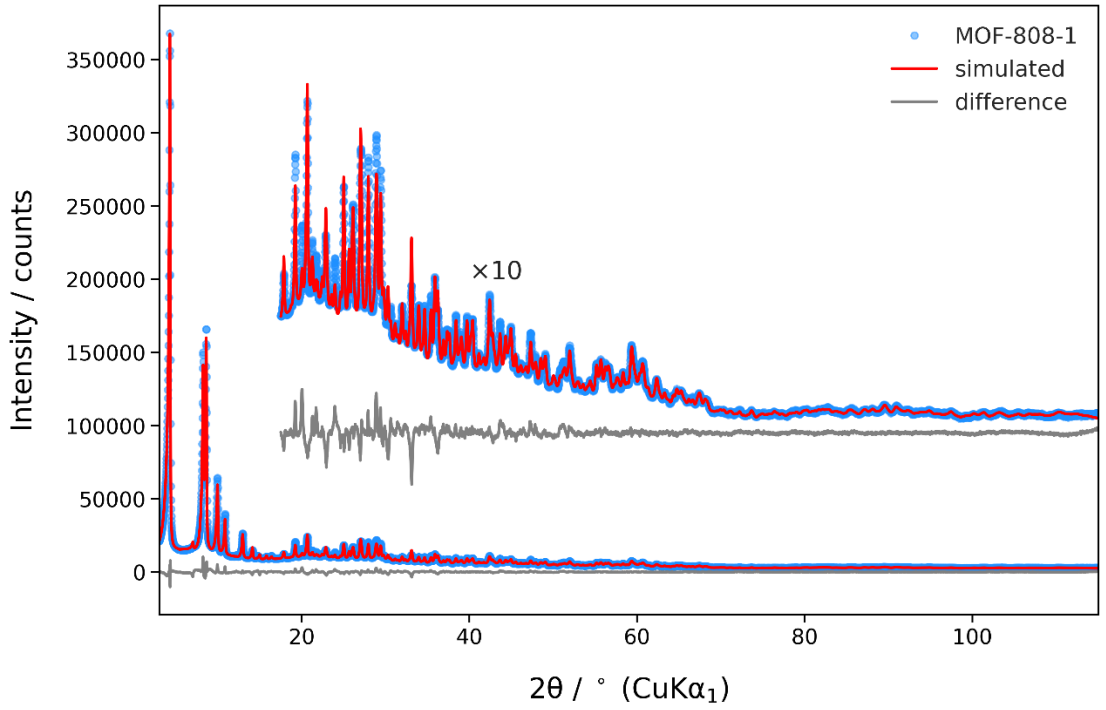

Figure S14. Rietveld refinement of bare MOF-808 X-ray total scattering data.

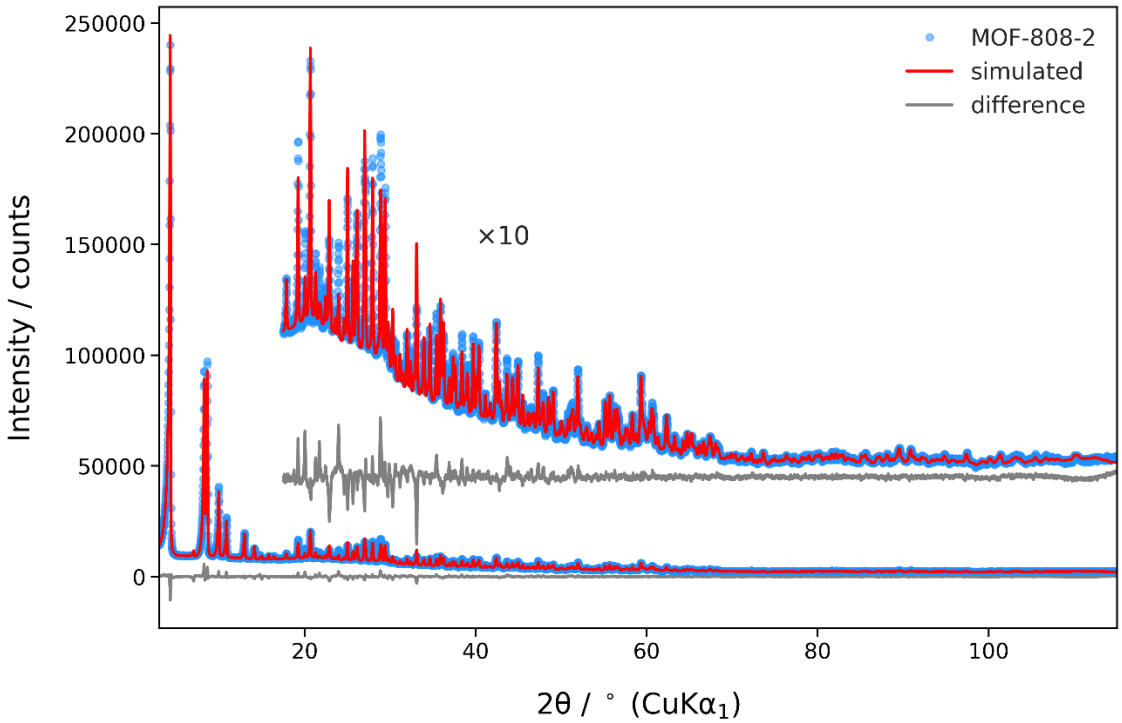

Figure S15. Rietveld refinement of iodate-loaded MOF-808 X-ray total scattering data.

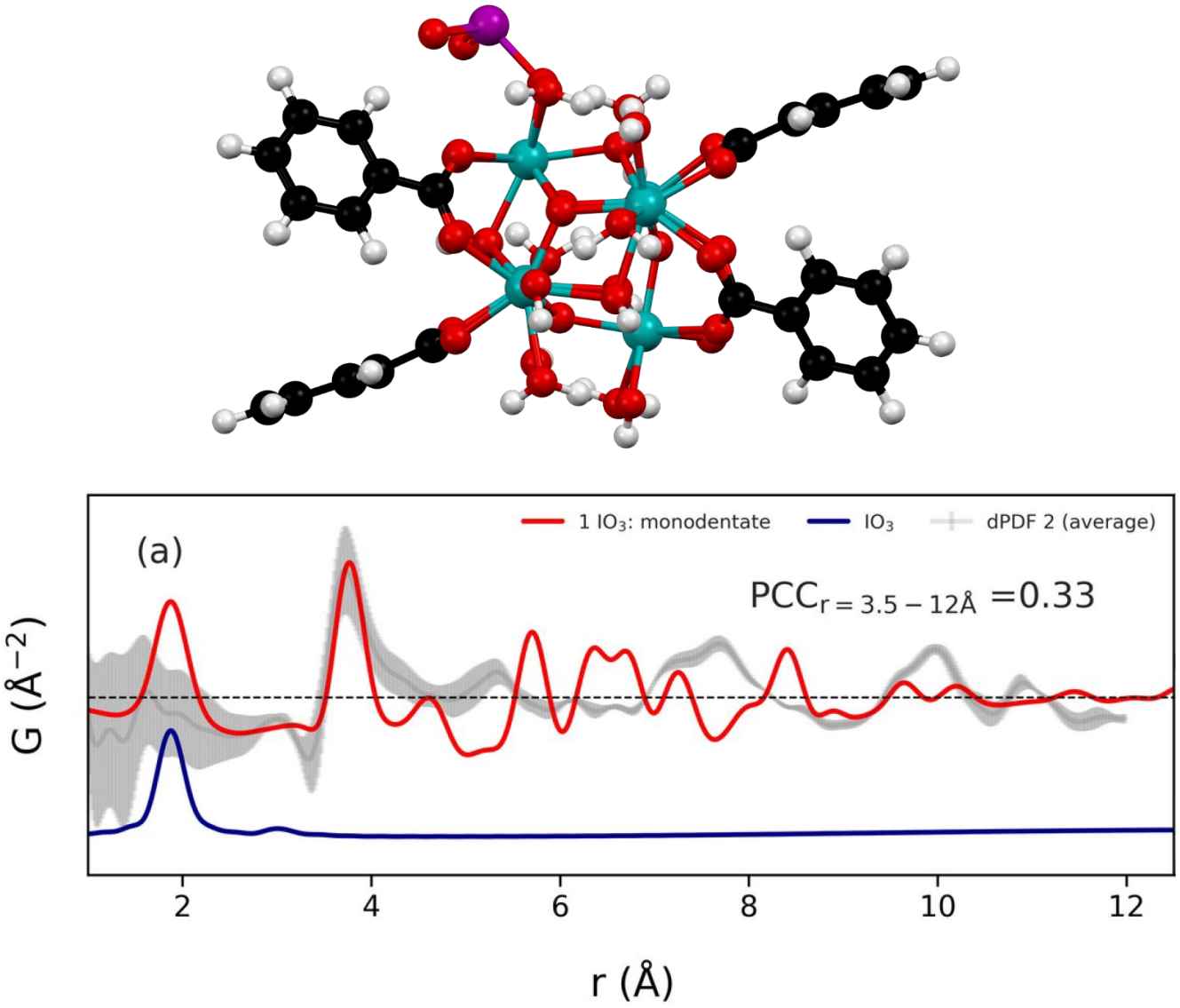

Figure S16. Optimized structural model of a single monodentate iodate binding to a MOF-808 Zr_6 node. The model's simulated dPDF (red) is overlaid on the experimentally obtained iodate-loaded MOF-808 dPDF (grey), and the simulated PDF of free iodate (blue).

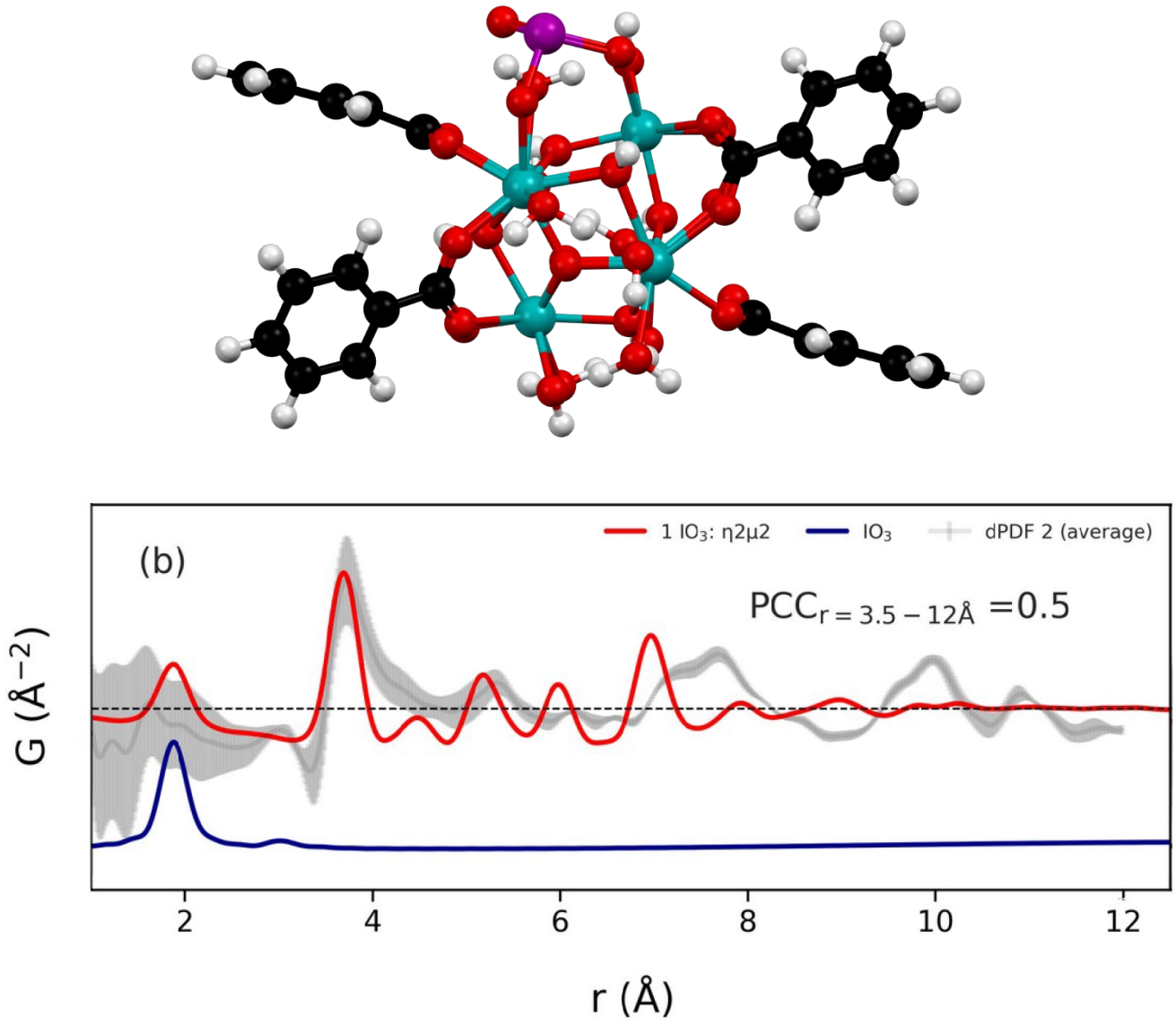

Figure S17. Optimized structural model of a single bridging iodate binding to a MOF-808 Zr_6 node. The model's simulated dPDF (red) is overlaid on the experimentally obtained iodate-loaded MOF-808 dPDF (grey), and the simulated PDF of free iodate (blue).

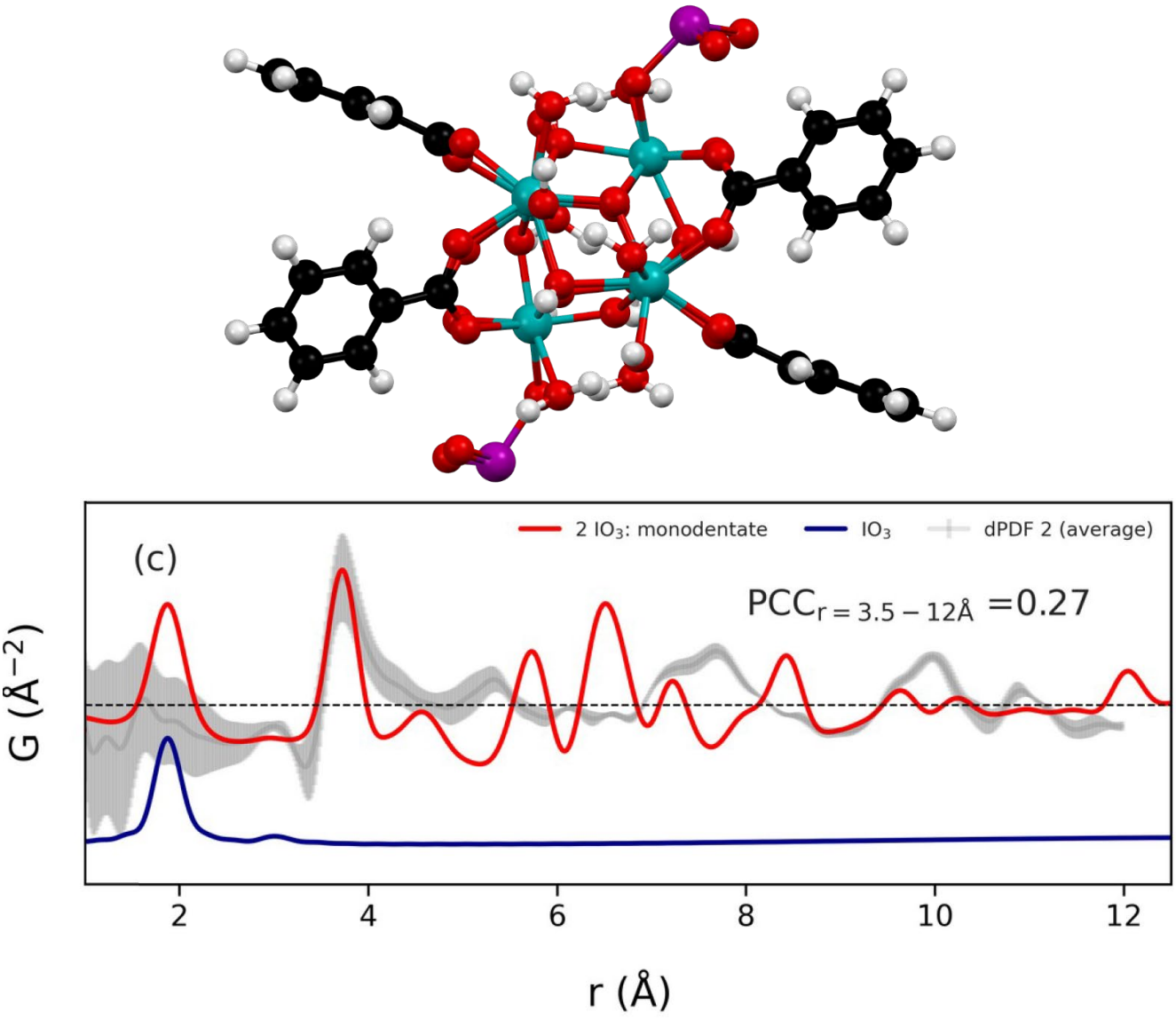

Figure S18. Optimized structural model of two bridging iodate anions binding to a MOF-808 Zr_6 node. The model's simulated dPDF (red) is overlaid on the experimentally obtained iodate-loaded MOF-808 dPDF (grey), and the simulated PDF of free iodate (blue).

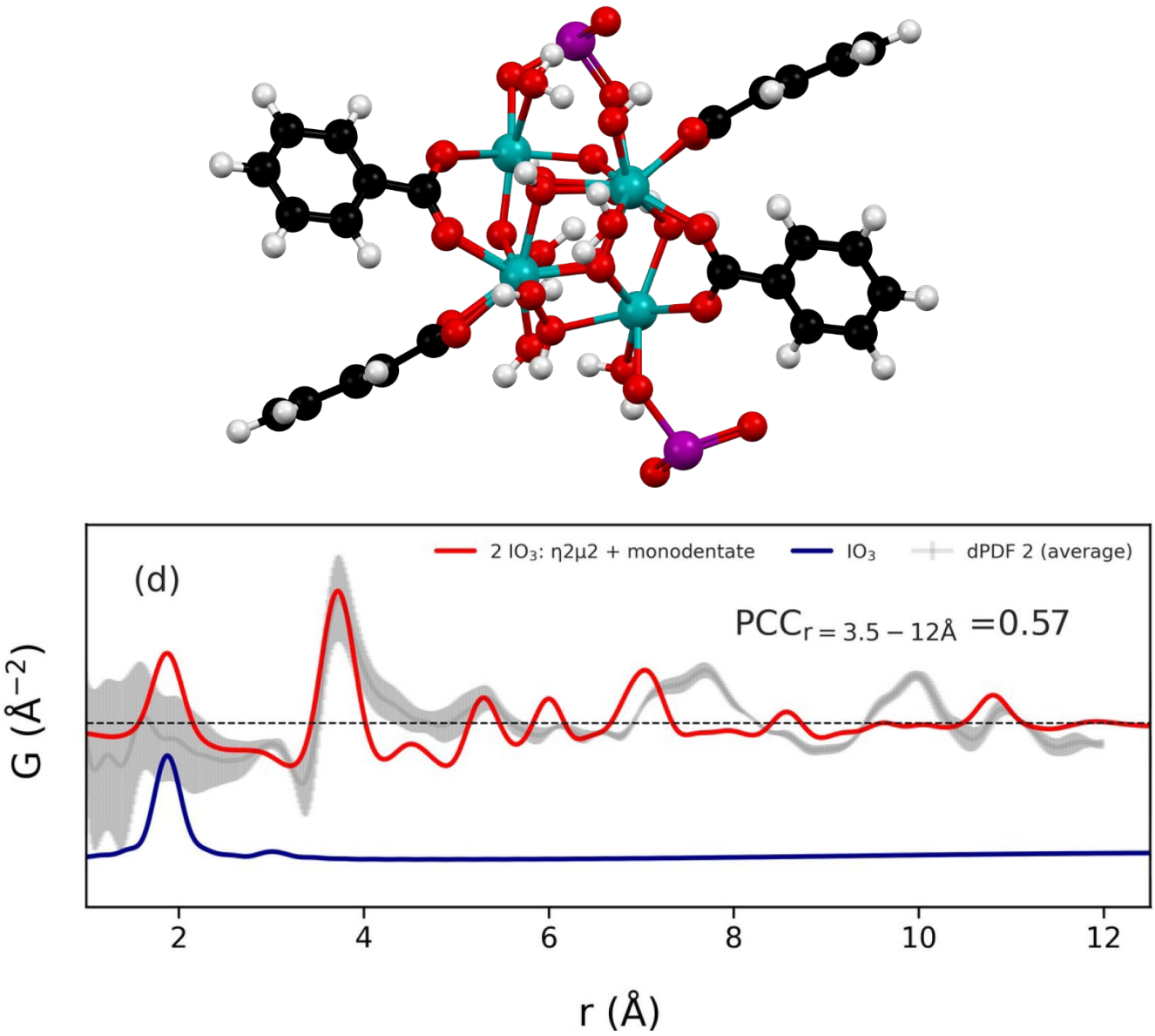

Figure S19. Optimized structural model of a monodentate and bridging iodate anion binding to opposite sides of a MOF-808 Zr_6 node. The model's simulated dPDF (red) is overlaid on the experimentally obtained iodate-loaded MOF-808 PDF (grey), and the simulated dPDF of free iodate (blue).

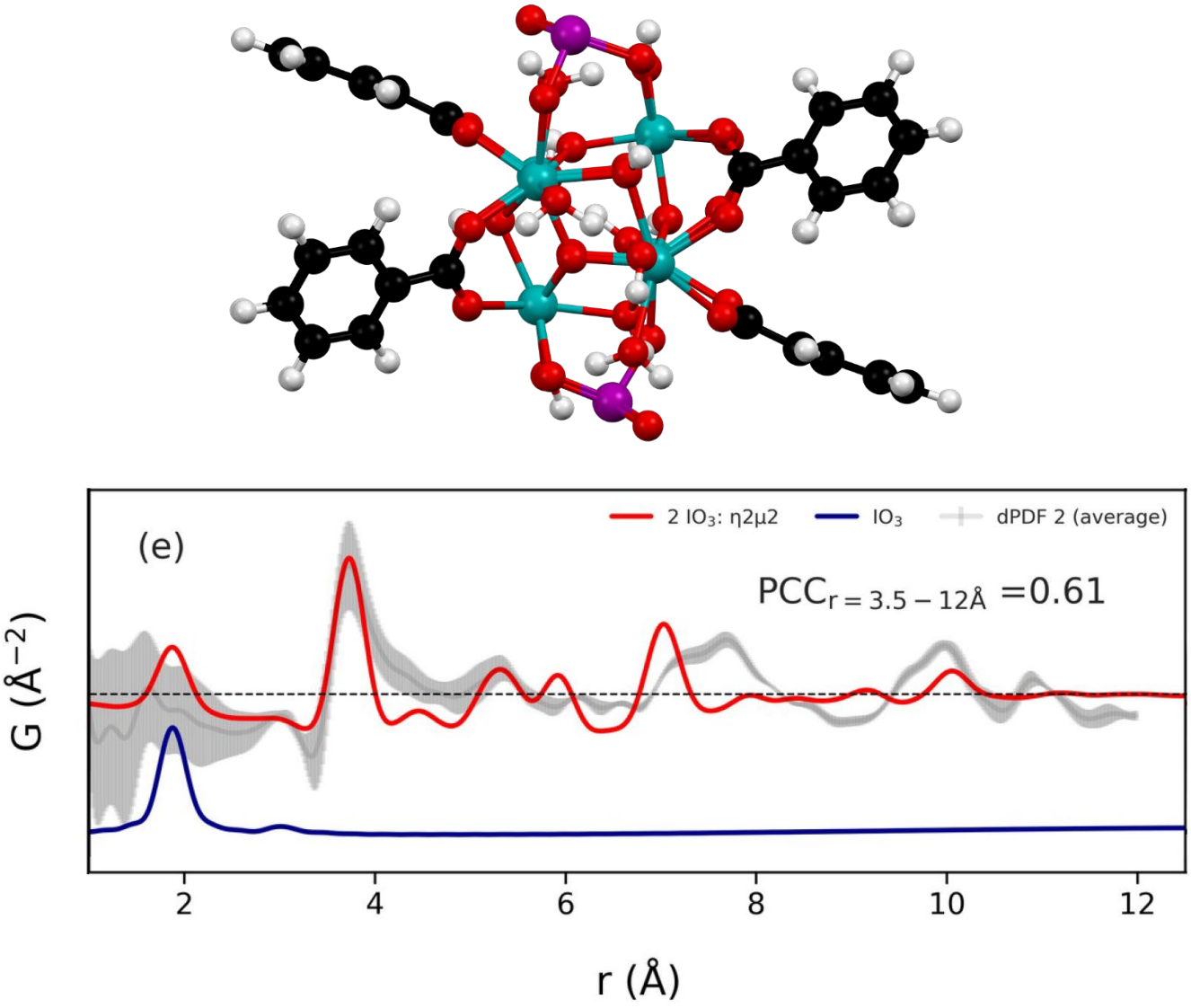

Figure S20. Optimized structural model of two bridging iodate anion binding to opposite sides of a MOF-808 Zr_6 node. The model's simulated dPDF (red) is overlaid on the experimentally obtained iodate-loaded MOF-808 dPDF (grey), and the simulated PDF of free iodate (blue).

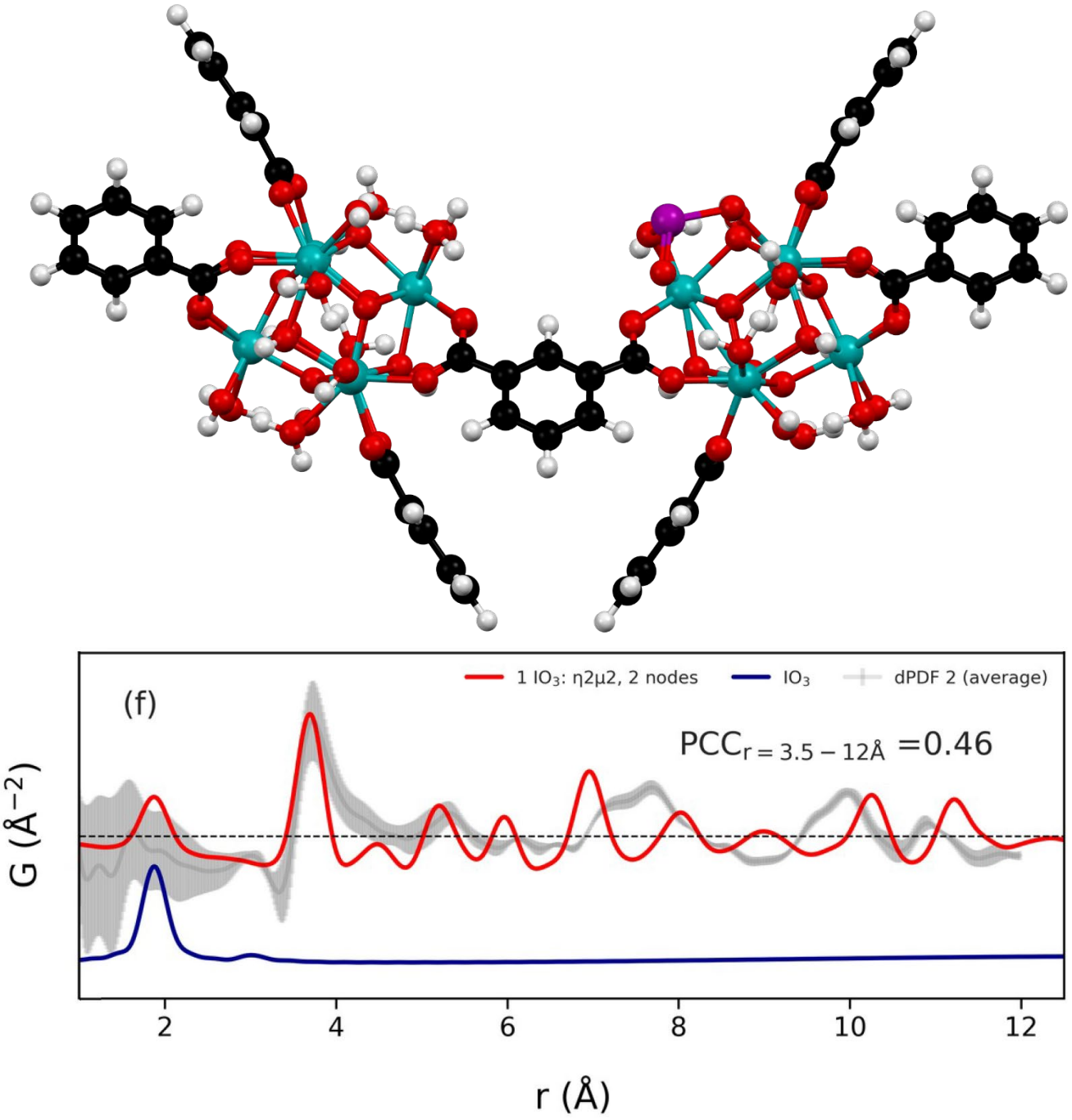

Figure S21. Optimized structural model of a bridging iodate anion binding to one Zr_6 node of a 2-node MOF-808 system. The model's simulated dPDF (red) is overlaid on the experimentally obtained iodate-loaded MOF-808 dPDF (grey), and the simulated PDF of free iodate (blue).

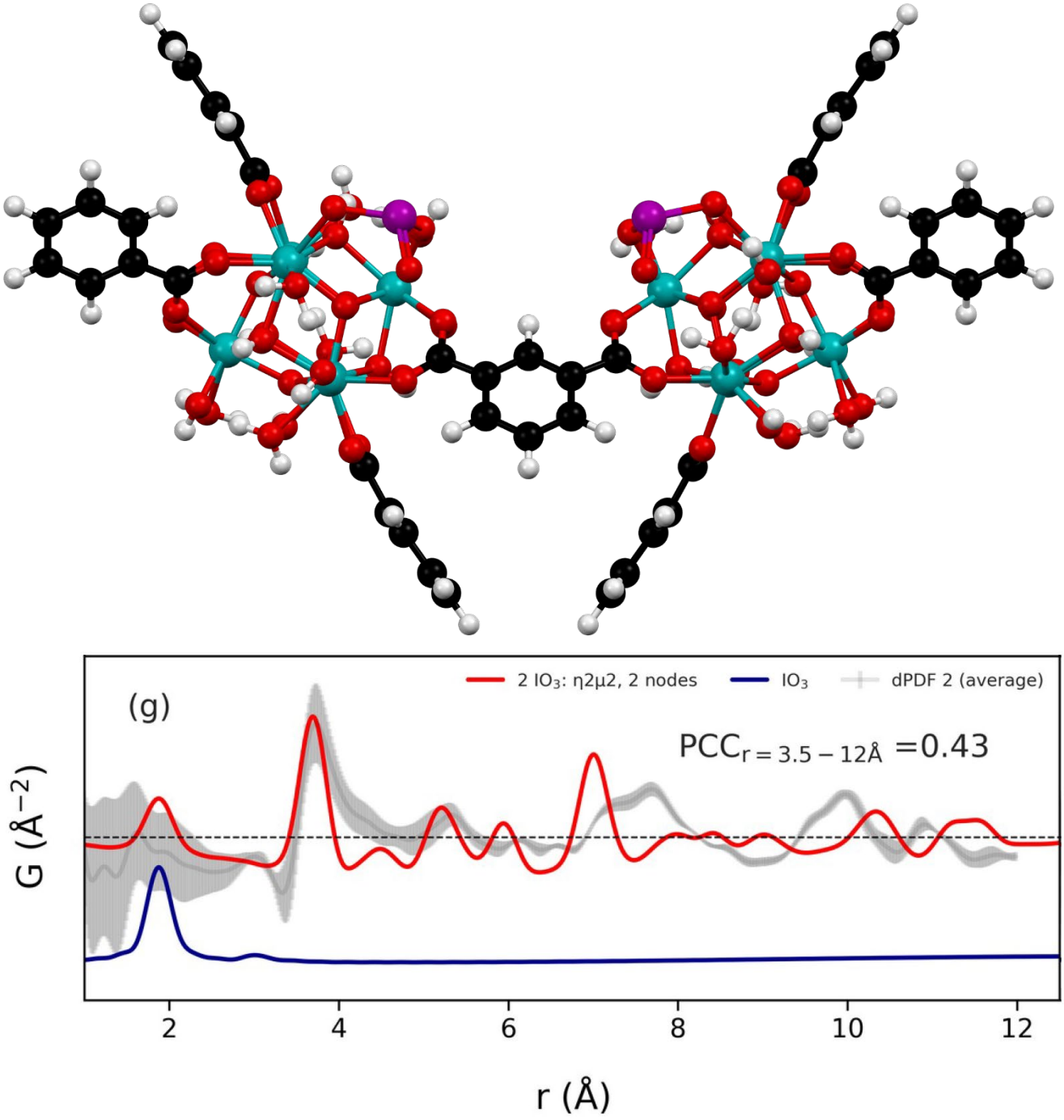

Figure S22. Optimized structural model of two bridging iodate anion binding to nearest adjacent sites on opposite Zr_6 nodes of a 2-node MOF-808 system. The model's simulated dPDF (red) is overlaid on the experimentally obtained iodate-loaded MOF-808 dPDF (grey), and the simulated PDF of free iodate (blue).

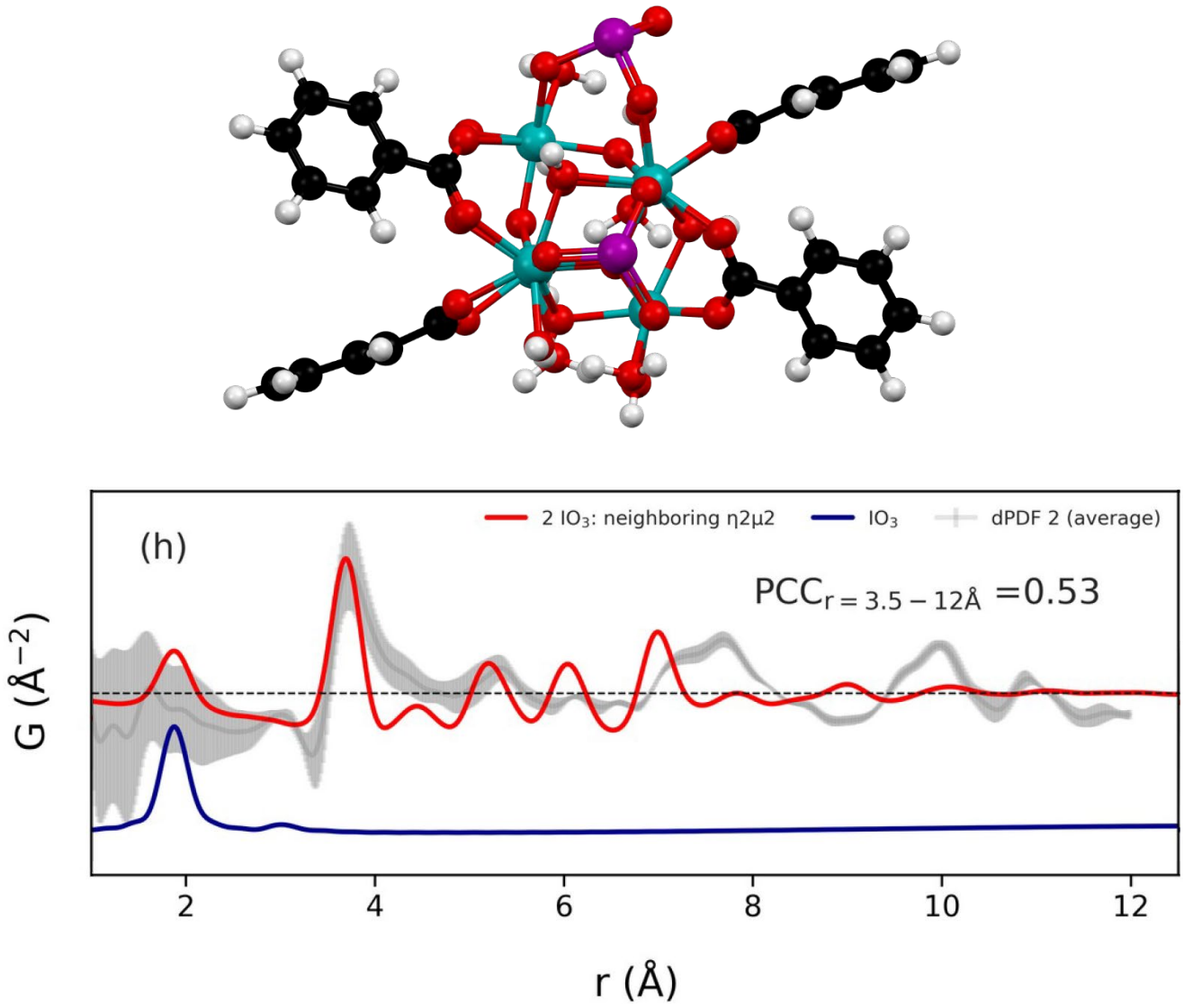

Figure S23. Optimized structural model of two bridging iodate anion binding to nearest sites on a MOF-808 Zr_6 node. The model's simulated dPDF (red) is overlaid on the experimentally obtained iodate-loaded MOF-808 dPDF (grey), and the simulated PDF of free iodate (blue).

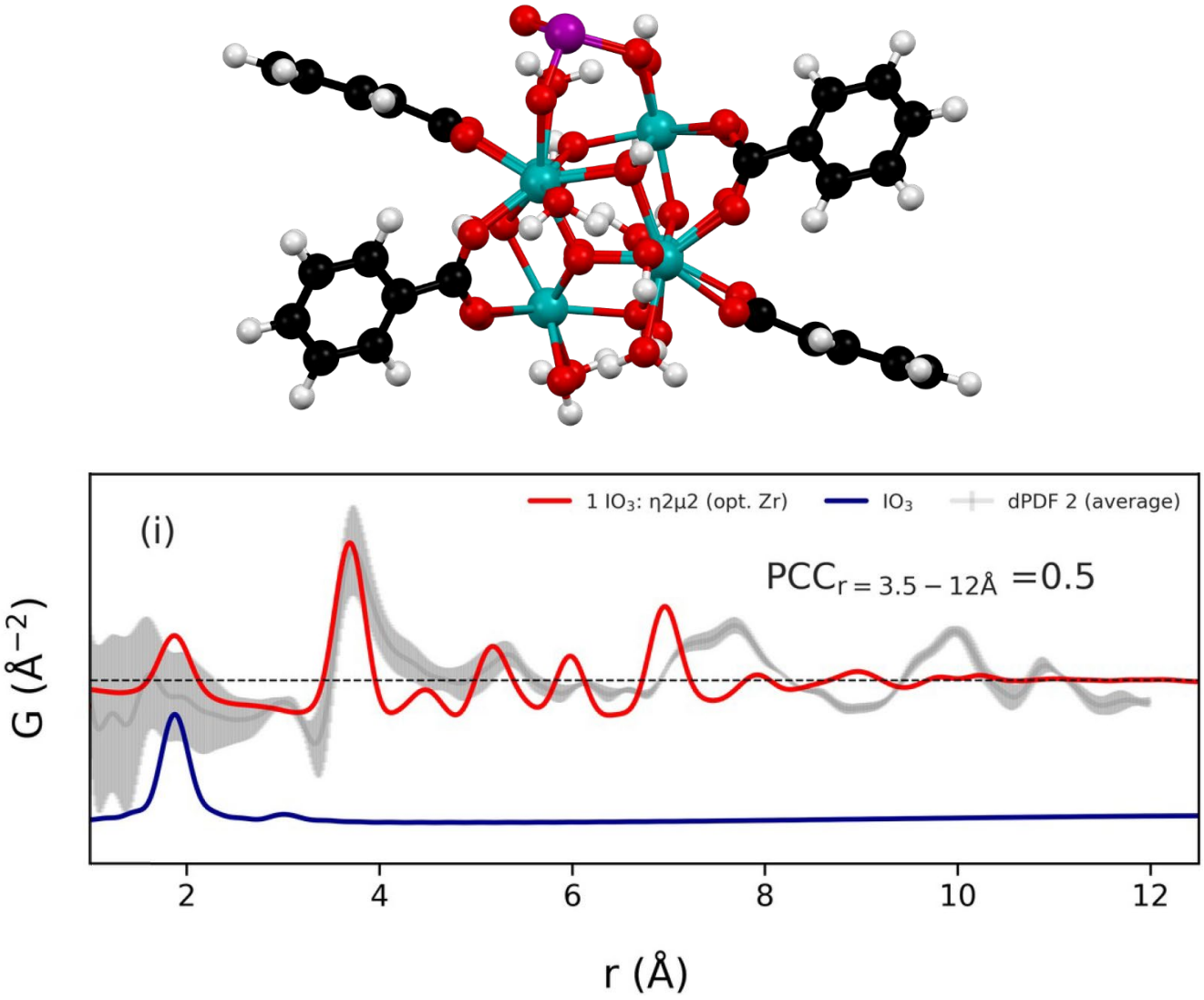

Figure S24. Optimized structural model of a bridging iodate anion binding to a MOF-808 Zr_6 node. Zr atomic coordinates were refined and frozen during optimization to account for any lattice distortions on binding. The model's simulated dPDF (red) is overlaid on the experimentally obtained iodate-loaded MOF-808 PDF (grey), and the simulated dPDF of free iodate (blue).

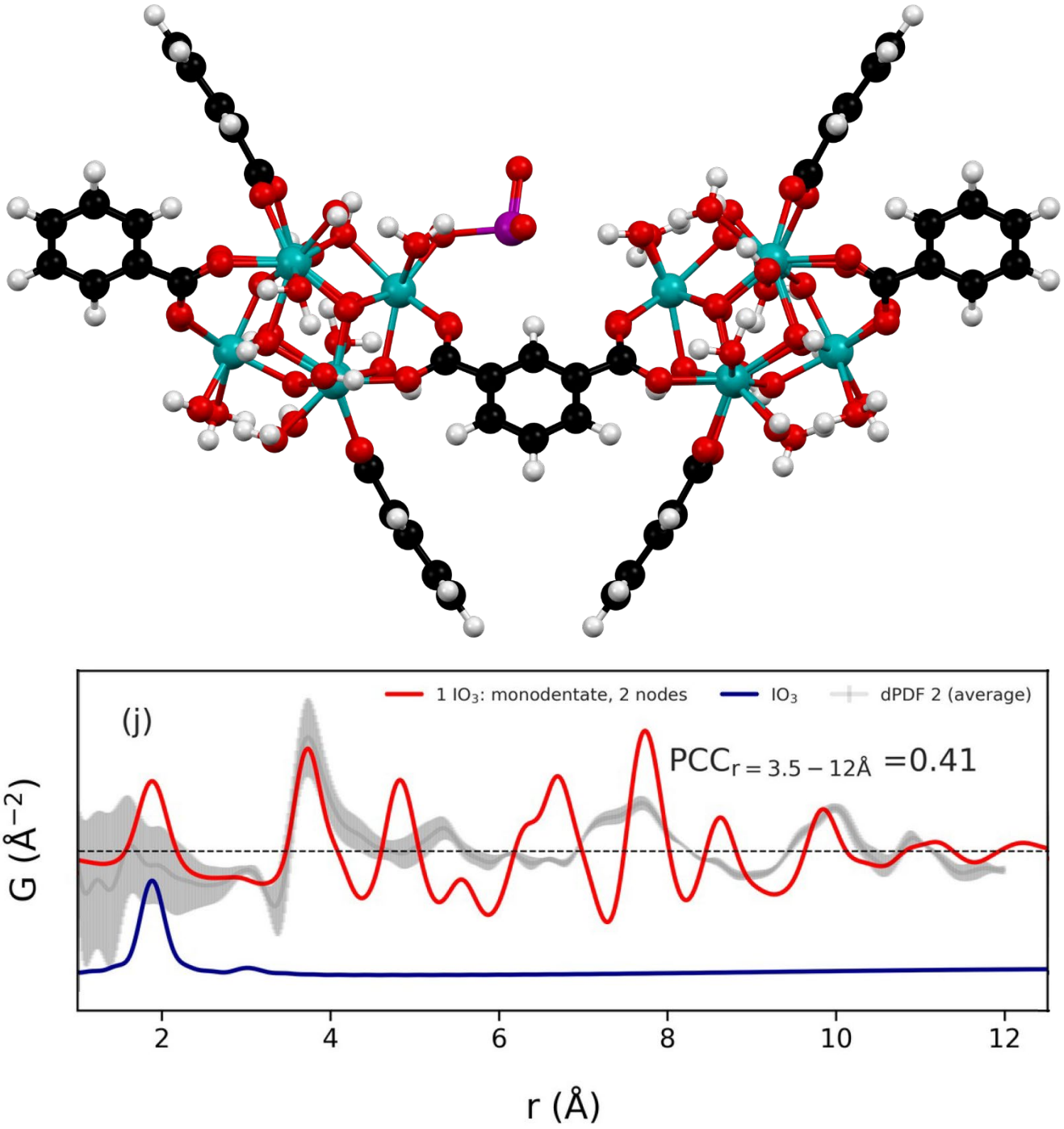

Figure S25. Optimized structural model of a monodentate iodate anion binding to one Zr_6 node of a 2-node MOF-808 system. The model's simulated dPDF (red) is overlaid on the experimentally obtained iodate-loaded MOF-808 dPDF (grey), and the simulated PDF of free iodate (blue).

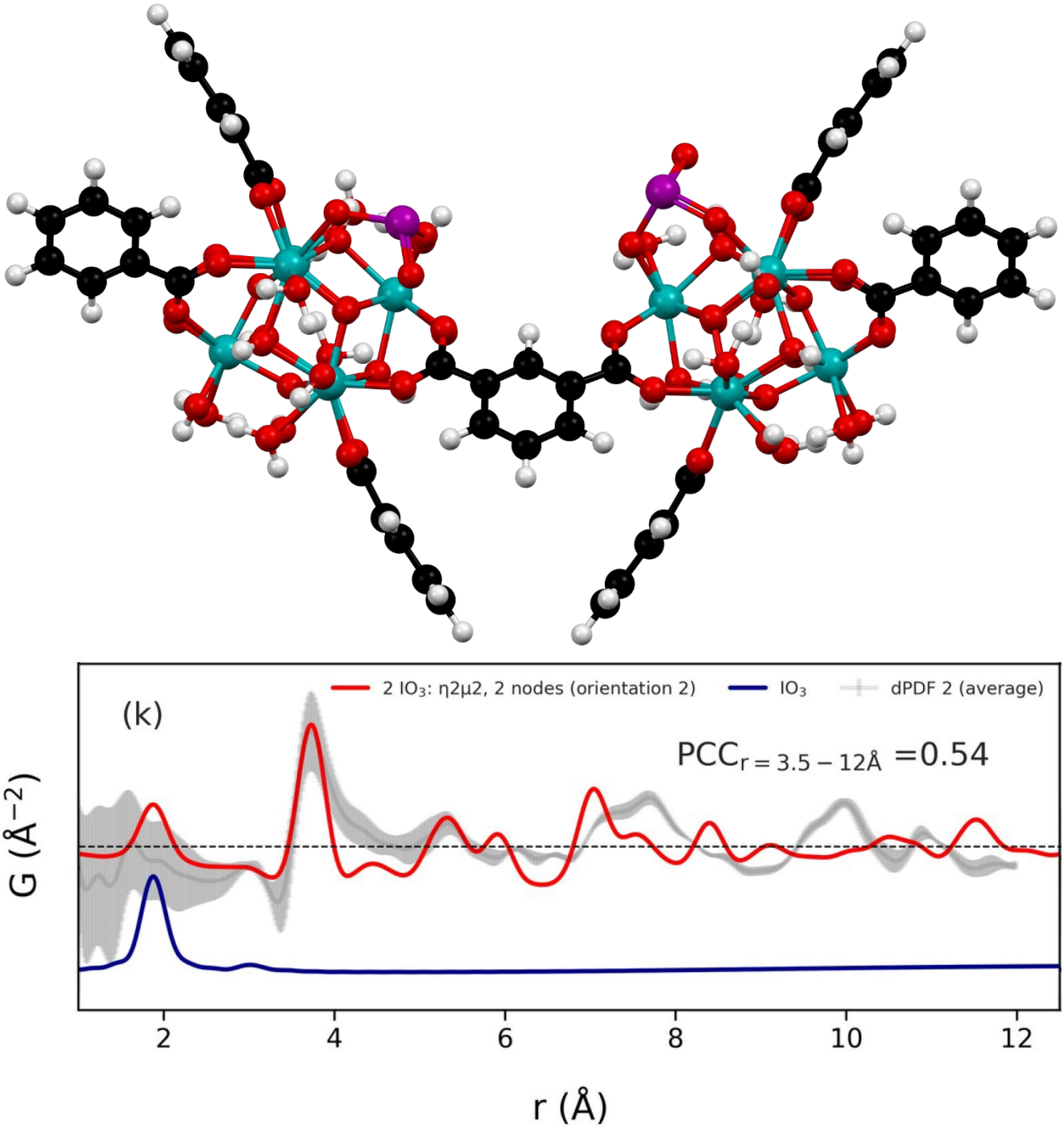

Figure S26. Optimized structural model of two bridging iodate anion binding to the second nearest adjacent sites on opposite Zr_6 nodes of a 2-node MOF-808 system. The model's simulated dPDF (red) is overlaid on the experimentally obtained iodate-loaded MOF-808 dPDF (grey), and the simulated PDF of free iodate (blue).

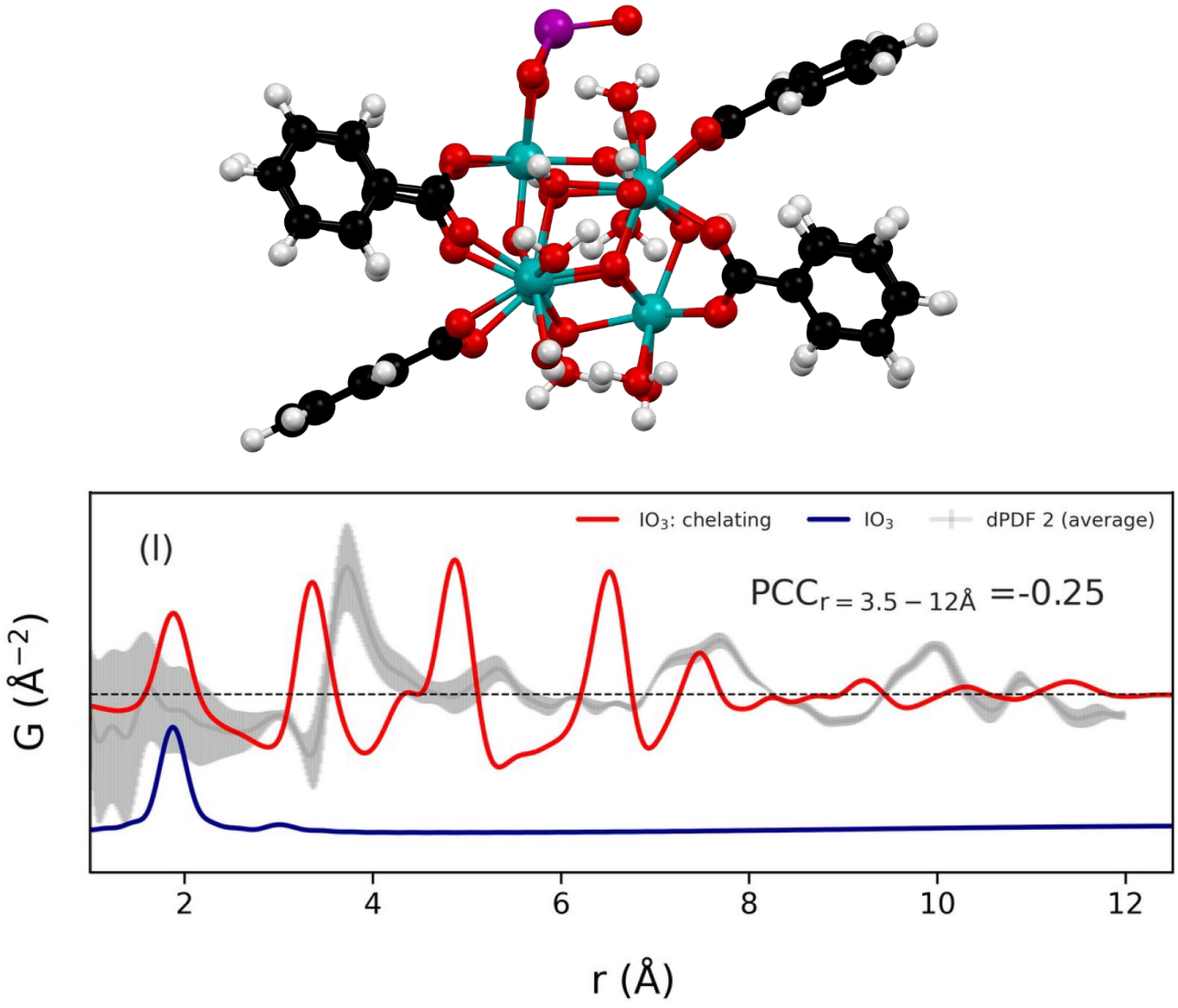

Figure S27. Optimized structural model of a single chelating iodate binding to a MOF-808 Zr_6 node, with its unbound oxygen facing towards the node. The model's simulated dPDF (red) is overlaid on the experimentally obtained iodate-loaded MOF-808 dPDF (grey), and the simulated PDF of free iodate (blue).

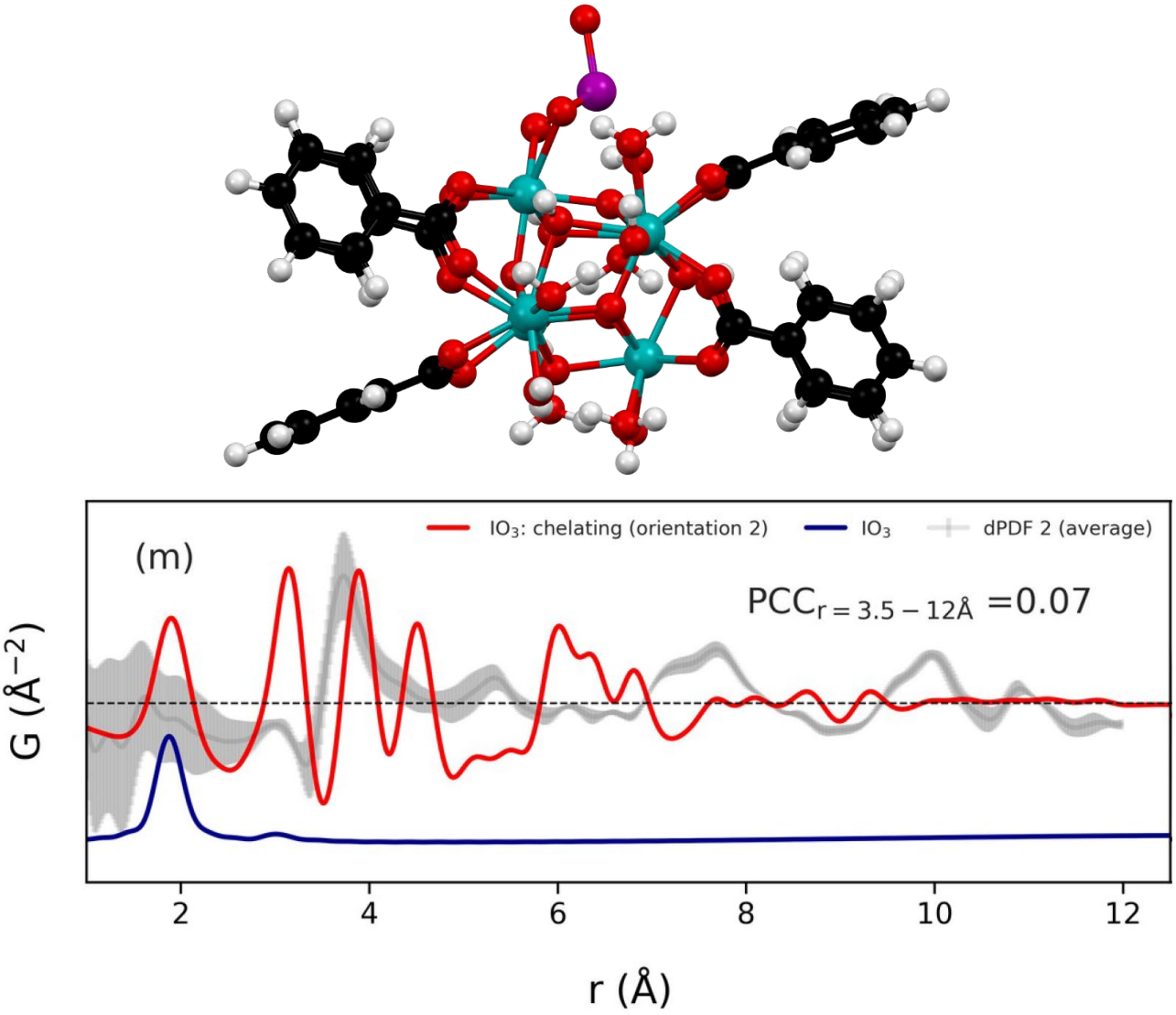

Figure S28. Optimized structural model of a single chelating iodate binding to a MOF-808 Zr_6 node, with its unbound oxygen facing away from the node. The model's simulated dPDF (red) is overlaid on the experimentally obtained iodate-loaded MOF-808 dPDF (grey), and the simulated PDF of free iodate (blue).

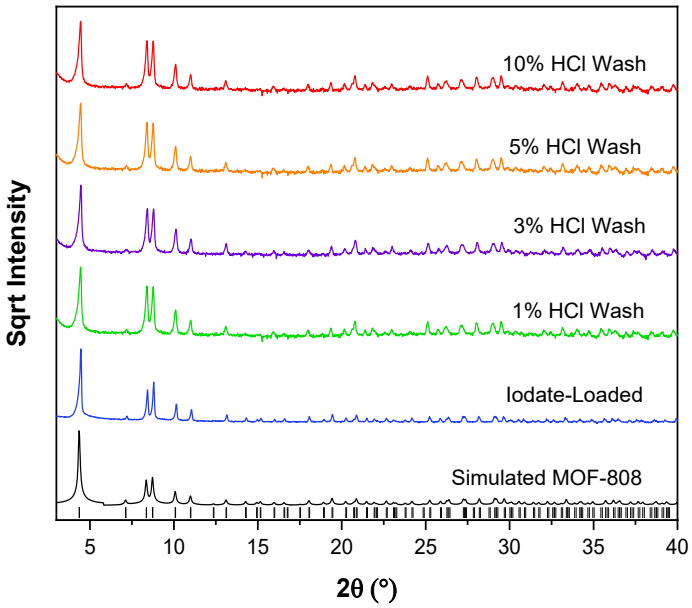

Figure S29. Powder X-ray diffraction patterns (CuKα, λ = 1.54178 Å) for MOF-808 including simulated, as-synthesized, and acid regenerated (1%, 3%, 5%, 10% HCl wash).

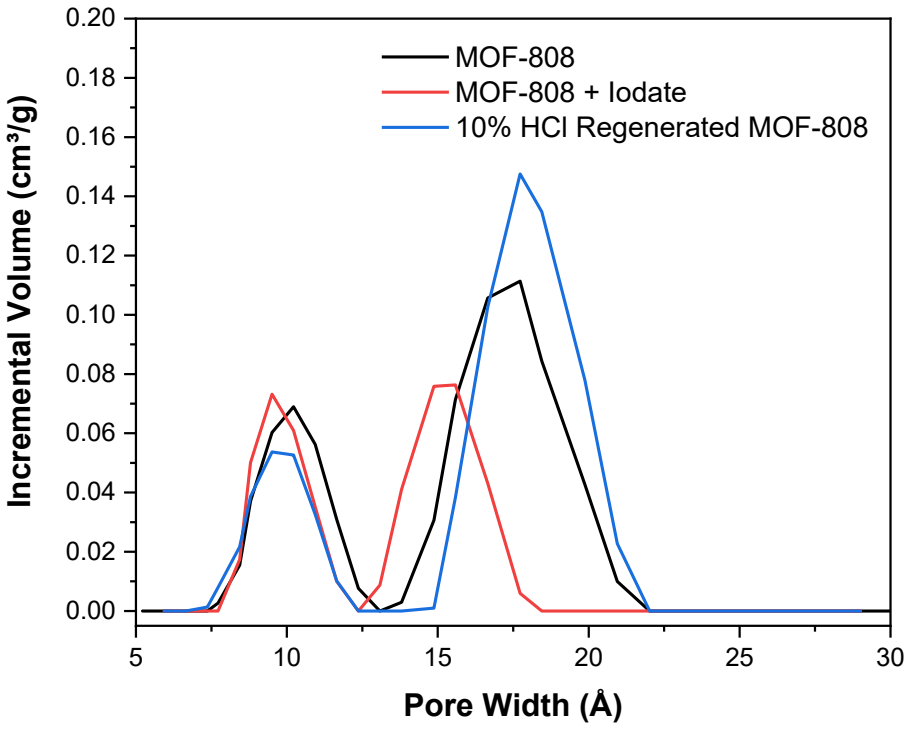

Figure S30. MOF-808 pore size distribution before iodate loading (black), loaded with iodate (red) and after regeneration with 10% HCl (blue).

1) H. Furukawa, F. Gándara, Y.-B. Zhang, J. Jiang, W. L. Queen, M. R. Hudson, and O. M. Yaghi, *J. Am. Chem. Soc.,* 2014, **136**, 4369-4381.
2) J. E. Mondloch, M. J. Katz, N. Planas, D. Semrouni, L. Gagliardi, J. T. Hupp and O. K. Farha, *Chem. Commun.*, 2014, **50**, 8944–8946.
3) R. J. Drout, A. J. Howarth, K. Otake, T. Islamoglu, and O. K. Farha. *CrystEngComm*, 2018, **20**, 6140-6145.
4) Z.-Q. Li, J.-C. Yang, K.-W. Sui and N. Yin, *Mater. Lett.*, 2015, **160**, 412–414.
5) S. Lin, Y. Zhao and Y.-S. Yun, *ACS Appl. Mater. Interfaces*, 2018, **10**, 28076–28085.
6) H.-B. Luo, M. Wang, S.-X. Liu, C. Xue, Z.-F. Tian, Y. Zou and X.-M. Ren, *Inorg. Chem.*, 2017, **56**, 4169–4175.
7) H.-Q. Zheng, C.-Y. Liu, X.-Y. Zeng, J. Chen, J. Lü, R.-G. Lin, R. Cao, Z.-J. Lin and J.-W. Su, *Inorg. Chem.*, 2018, **57**, 9096–9104.
8) H. G. T. Ly, G. Fu, A. Kondinski, B. Bueken, D. De Vos and T. N. Parac-Vogt, *J. Am. Chem. Soc.*, 2018, **140**, 6325–6335.
9) S. Dai, C. Simms, I. Dovgaliuk, G. Patriarche, A. Tissot, T. N. Parac-Vogt and C. Serre, *Chem. Mater.*, 2021, **33**, 7057–7066.
10) S. Karmakar, S. Barman, F. Ahamed Rahimi and T. Kumar Maji, *Energy Environ. Sci.*, 2021, **14**, 2429–2440.
11) A. A. Oliveira, L. C. Trevizan, and J. A. Nóbrega, *Appl. Spectrosc. Rev*. 2010, **45** (6), 447–473.
12) M. J. Frisch, G. W. Trucks, H. B. Schlegel, G. E. Scuseria, M. A. Robb, J. R. Cheeseman, G. Scalmani, V. Barone, B. Mennucci, G. A. Petersson, H. Nakatsuji, M. Caricato, X. Li, H. P Hratchian, A. F. Izmaylov, J. Bloino, G. Zheng, J. L. Sonnenberg, M. Hada, M. Ehara, K. Toyota, R. Fukuda, J. Hasegawa, M. Ishida, T. Nakajima, Y. Honda, O. Kitao, H. Nakai, T. Vreven, J. A. Montgomery Jr, J. E. Peralta, F. β. Ogliaro, M. J. Bearpark, J. Heyd, E. N. Brothers, K. N. Kudin, V. N. Staroverov, R. Kobayashi, J. Normand, K. Raghavachari, A. P. Rendell, J. C. Burant, S. S. Iyengar, J. Tomasi, M. Cossi, N. Rega, N. J. Millam, M. Klene, J. E. Knox, J. B. Cross, V. Bakken, C. Adamo, J. Jaramillo, R. Gomperts, R. E. Stratmann, O. Yazyev, A. J. Austin, R. Cammi, C. Pomelli, J. W. Ochterski, R. L. Martin, K. Morokuma, V. G. Zakrzewski, G. A. Voth, P. Salvador, J. J. Dannenberg, A. Dapprich, A. D. Daniels, ñ. n. Farkas, J. B. Foresman, J. V. Ortiz, J. Cioslowski and D. J. Fox, Gaussian, Inc.: Wallingford, CT, USA, 2009.
13) P. J. Chupas, X. Qiu, J. C. Hanson, P. L. Lee, C. P. Grey and S. J. L. Billinge, *J. Appl. Crystallogr.* 2003, **36**, 1342–1347.
14) C. L. Farrow, P. Juhás, J. Liu, D. Bryndin, E. S. Božin, J. Bloch, T. Proffen and S. J. L. Billinge, *J. Phys. Condens. Matter.* 2007, **19**, 335219.
15) J. Kieffer, G. Ashiotis, A. Deschildre, Z. Nawaz, J. P. Wright, D. Karkoulis and F. E. Picca, F. E, 2015, **48**, 510–519.
16) P. Juhás, T. Davis, C. L. Farrow, and S. J. L. Billinge, *J. Appl. Crystallogr.* 2013, **46**, 560–566.
17) X. Yang, P. Juhás, C. L. Farrow and S. J. L. Billinge, *arXiv.* 2015, 1402.3163.
18) C. L. Farrow and S. J. L. Billinge, *Acta Crystallogr. A* 2009, **65**, 232–239.
19) P. Juhás, C. L. Farrow, X. Yang, K. R. Knox and S. J. L Billinge, *Acta Crystallogr. A* 2015, **71**, 562– 568.

20)E. Lorch, *J. Phys. C: Solid State Phys.* 1969, **2**, 229–237.
21)M. W. Terban, S. K. Ghose, A. M. Plonka, D. Troya, P. Juhás, R. E. Dinnebier, J. J. Mahle, W. O. Gordon,and A. I. Frenkel, *Commun. Chem.* 2021, **4**, 2.
22)A. A. Coelho, *J. Appl. Crystallogr.* 2018, **51**, 210–218.
23) T. Da, and T. Chen. *J. Radioanal. Nucl. Chem.,* 2020**, 326**, 511–523.
24) Q. Zhao, G. Chen, Z. Wang, M. Jiang, J. Lin, L. Zhang, L. Zhu, and T. Duan. *Chem. Eng.J.* 2021, **426**, 131629.
25) T.-X. Da, T. Chen, W.-K. He, P. Liu, Y. Ma, and Z.-F. Tong, *J. Radioanal. Nucl. Chem.,* 2021, **329** (3), 1277–1290.
26) W. Yu, H. Xu, D. Tan, Y. Fang, E. E. Roden, and Q Wan. *Appl. Clay Sci.* 2020, **184**, 105407.
27) D. Li, D. I. Kaplan, A. Sams, B. A. Powell, and A. S. Knox. *J. Environ. Radioact.* 2018, **192**, 505–512.
28) R. Mahmudov, and C.P. Huang, C. P. *Sep. Purif. Technol.,* 2011, **77** (3), 294–300.
29) J. L. Dai, M. Zhang, Q. H. Hu, Y. Z. Huang, R. Q. Wang, and Y. G. Zhu. *Geoderma* 2009, **153** (1), 130–135.